

# A Tail of Two Populations: Chemo-dynamics of the Sagittarius Stream and Implications for Its Original Mass

S.L.J. Gibbons<sup>1\*</sup>, V. Belokurov<sup>1</sup> and N.W. Evans<sup>1</sup>

<sup>1</sup>*Institute of Astronomy, University of Cambridge, Madingley Road, Cambridge, CB3 0HA, UK*

Accepted Received ; in original form

## ABSTRACT

We use the SDSS/SEGUE spectroscopic sample of stars in the leading and trailing streams of the Sagittarius (Sgr) to demonstrate the existence of two sub-populations with distinct chemistry and kinematics. The metallicity distribution function (MDF) of the trailing stream is decomposed into two Gaussians describing a metal-rich sub-population with means and dispersions  $(-0.74, 0.18)$  dex and a metal-poor with  $(-1.33, 0.27)$  dex. The metal-rich sub-population has a velocity dispersion  $\sim 8 \text{ km s}^{-1}$ , whilst the metal-poor is nearly twice as hot  $\sim 13 \text{ km s}^{-1}$ . For the leading stream, the MDF is again well-described by a superposition of two Gaussians, though somewhat shifted as compared to the trailing stream. The metal-rich has mean and dispersion  $(-1.00, 0.34)$  dex, the metal-poor  $(-1.39, 0.22)$  dex. The velocity dispersions are inflated by projection effects to give 15 - 30  $\text{kms}^{-1}$  for the metal-poor, and 6 - 20  $\text{kms}^{-1}$  for the metal-rich, depending on longitude. We infer that, like many dwarf spheroidals, the Sgr progenitor possessed a more extended, metal-poor stellar component and less extended, metal-rich one. We study the implications of this result for the progenitor mass by simulating the disruption of the Sgr, represented as King light profiles in dark halos of masses between  $10^{10}$  and  $10^{11} M_{\odot}$ , in a three-component Milky Way whose halo is a live Truncated Flat potential in the first phase of accretion and a triaxial Law & Majewski model in the second phase. We show that that the dark halo of the Sgr must have been  $\gtrsim 6 \times 10^{10} M_{\odot}$  to reproduce the run of velocity dispersion with longitude for the metal-rich and metal-poor sub-populations in the tails.

**Key words:** Galaxy: halo – galaxies: kinematics and dynamics – galaxies: individual: Sagittarius

## 1 INTRODUCTION

The disruption of the third most massive satellite of the Galaxy, the Sagittarius dwarf (Sgr) is currently in full swing. Its tidal debris has been sprayed all over the sky in a theatrical demonstration of the messy eating habits of the more massive Milky Way (MW) Galaxy. Exemplifying the hierarchical nature of structure assembly on small scales, the Sgr accretion event has been used to champion the  $\Lambda$ CDM theory. Over the last decade, its tidal tails have been mapped across a large Galactic volume and have been utilized to study the matter distribution in the Milky Way. However, there remain embarrassing lacunae that threaten to mar the stream based inference procured so far: we know neither the Sgr’s original mass nor where the dwarf came from.

In fact, as shown by Jiang & Binney (2000), the Sgr mass and the initial apocentric distance of its orbit are tightly linked. The current position of the remnant can be reproduced by a large range of initial conditions from low apocentres at around 60 kpc to those be-

yond the virial radius of the Milky Way, i.e.,  $> 200$  kpc. On one end of the spectrum, low size orbits are allowed to exist coupled with a light Sgr dwarf with  $M \sim 10^9 M_{\odot}$ ; on the other hand, a substantially heavier Sgr with  $M \sim 10^{11} M_{\odot}$  could plausibly start much further away, but then sink quickly into the central Galaxy thanks to dynamical friction with the MW’s dark halo. Thus, the dynamical modeling permits an uncertainty of two orders of magnitude in mass. Unfortunately, this cannot be improved through direct observation: the original properties of the dwarf and its orbit are simply not available today. There are however indirect indications that can be invoked to help deduce what the progenitor’s mass might have been.

Law & Majewski (2010b) attempt to address the Sgr mass conundrum by taking advantage of the measurement of the velocity dispersion of the trailing tail debris. They conjecture that a more massive progenitor ought to host a stellar population with a higher intrinsic velocity dispersion that would produce a hotter tidal stream on disruption – a hypothesis they convincingly prove to be correct with a suite of numerical simulations of the Sgr disruption. Note that only a simple one-component (representing both DM and

\* E-mail: sljg2,vasily,nwe@ast.cam.ac.uk

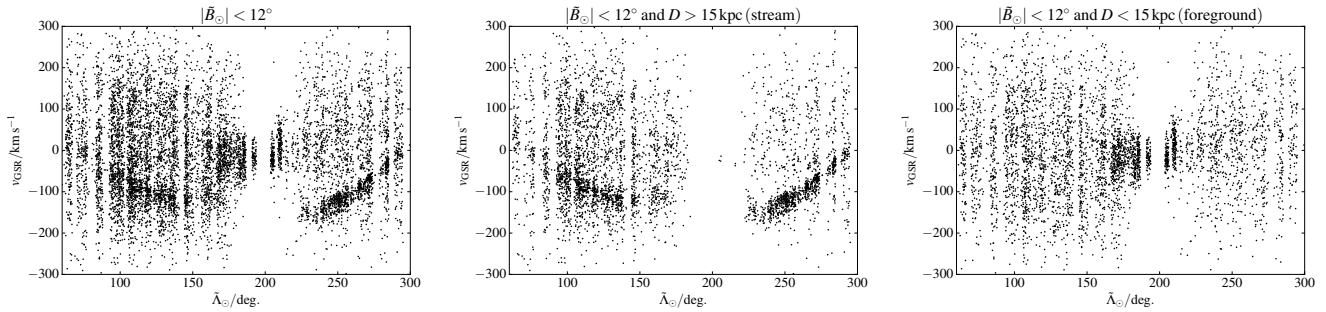


**Figure 1.** Our sample of SDSS/SEGUE stars focused on the Sagittarius Stream in the  $v_{\text{GSR}}$  versus  $\bar{\Lambda}_{\odot}$  plane. We show the selection before (left panel) and after (middle panel) the application of the distance cut, as well as the stars removed by the distance cut (right panel). The leading stream is visible as the overdensity with  $\bar{\Lambda}_{\odot} < 150^{\circ}$ . The trailing stream is the overdensity with  $\bar{\Lambda}_{\odot} > 220^{\circ}$ . The distance cut significantly reduces Milky Way contamination, whilst leaving the stream signal intact.

stars) model for the progenitor was used. Nonetheless, encouraged by the clear correlation between the stream’s dispersion and the progenitor’s mass, they relied on the most precise measurement of the Sgr debris dispersion available at the time. This was established by Monaco et al. (2007), who used high-resolution spectroscopy of the Sgr trailing tail giant stars to infer the dispersion of  $8.3 \pm 0.9 \text{ km s}^{-1}$ . Given the ensemble of models produced by Law & Majewski (see e.g. 2010b), the corresponding Sgr progenitor’s mass is  $6.4 \times 10^8 M_{\odot}$ , assuming the disruption duration of 8 Gyr.

There are (at least) three serious problems with such a low estimate of the original mass of the dwarf. First, as implied by the analysis of Jiang & Binney (2000), such a light Sgr does not have enough mass to experience any significant dynamical friction during its evolution in the MW potential. Therefore, it must have started its orbit at around 60 kpc from the Galactic centre, i.e. around its current apocentre. Note that the present day apocentre is fixed by the precise knowledge of the apocentres of the leading and trailing tails (see e.g. Belokurov et al. 2014). Cosmologically speaking, this makes little sense. The accretion of Sgr is a relatively recent event, dating back only to approximately  $z \sim 0.6$ . The most compelling evidence in this regard comes from the studies of the dwarf’s stellar populations. An approximate scale for the time elapsed since the beginning of the disruption is set by the M giants found in the Sgr trailing tail: their age is bracketed to lie between 4 and 9 Gyr (see e.g. Bellazzini et al. 2006). This is in agreement with de Boer et al. (2015) who demonstrate that the star formation activity in the stream ceased abruptly between 5 and 7 Gyr ago. Since  $z \sim 0.6$ , the Milky Way’s DM mass within the virial radius has experienced only a minuscule increase (see e.g. Diemer et al. 2013; Wetzel & Nagai 2015), thus rendering the turn-around radius of 60 kpc implausible.

Furthermore, the progenitor’s mass of  $\sim 6 \times 10^8 M_{\odot}$  appears inconsistent with the most recent estimate of the remnant’s current mass. Through modeling of a large sample of high-resolution NIR spectra as part of the APOGEE survey, Majewski et al. (2013) have gauged the remnant’s mass to be in the range  $5 - 7 \times 10^8 M_{\odot}$ . In other words, after 6-8 Gyr of continuous tidal stripping, the remnant’s mass today is claimed to be of order of the original progenitor’s mass! Finally, the dwarf’s mass before disruption can be guessed if its original luminosity was known. Niederste-Ostholt et al. (2010) provide exactly such an estimate. By carefully unpicking the Sgr tidal debris from the foreground stellar populations across the entire sky, they calculate the lower limit to the total stellar mass in the Sgr progenitor. According to Niederste-Ostholt et al.

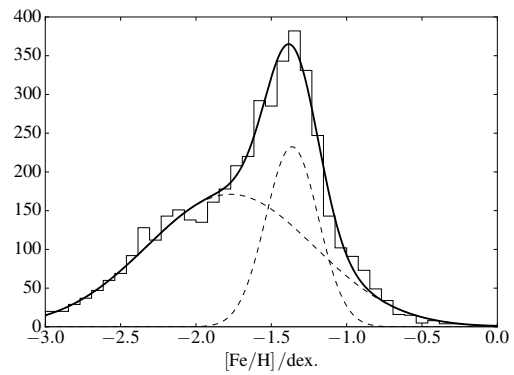


**Figure 2.** The MDF of all SDSS/SEGUE stars satisfying our selection that are located off the Sagittarius Stream ( $|\bar{B}_{\odot}| \geq 15^{\circ}$ ). It is well fit by two Gaussians (solid black curve) with components indicated by the dashed black lines.

(2010) and considering the analysis presented in Niederste-Ostholt et al. (2012), Sgr at infall must have contained  $\sim 1.4 \times 10^8 M_{\odot}$  in stars alone. Guided by the abundance matching relations (see e.g. Conroy & Wechsler 2009; Behroozi et al. 2010), the corresponding halo mass should be of order of  $10^{11} M_{\odot}$ .

Taking into account the arguments above, it is more likely that the Sgr dwarf’s original mass was much larger, i.e. closer to  $10^{11} M_{\odot}$ . Such a heavy Sgr would of course wreak havoc in the Milky Way’s disk. As pointed out by Jiang & Binney (2000), the Galaxy’s HI layer should show clear signs of interaction with the most massive of their versions of the dwarf. Naturally, the disk’s stellar component is likely to be disturbed just as well. Observationally, there are, actually, signs of such disturbances in both the neutral hydrogen layer – as represented by the spiral arms and the warp – and the stellar disk, as evidenced by the discovery of the wave-like oscillations in the Sloan Digital Sky Survey (SDSS) star counts (Widrow et al. 2012; Yanny & Gardner 2013). The link between the Sgr accretion and sub-structures in the disk has been recently firmed up through numerical simulations. For example, Purcell et al. (2011) establish connection between the Sgr infall and the Galactic spiral structure, while Gómez et al. (2016) identify the Sgr dwarf as their likely candidate to kick out large numbers of disk stars to form Monoceros ring-like structures.

A Sgr progenitor significantly more massive than that proposed by Law & Majewski (2010b) would superficially be in ten-

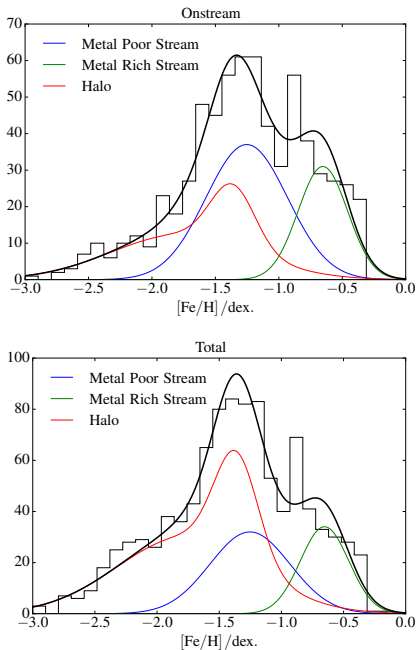


**Figure 3.** The upper panel shows the MDF of the stars in the trailing stream, with  $235^\circ \leq \tilde{\Lambda}_\odot \leq 274^\circ$ , and velocities within  $\pm 45 \text{ km s}^{-1}$  of the mean stream velocity. The green and blue lines show the metal-rich and metal-poor Sgr components, while the red line shows the contribution from the Milky Way component. The lower panel shows all the stars within the aforementioned range of  $\tilde{\Lambda}_\odot$ , with the components rescaled.

sion with the low velocity dispersion measured by Monaco et al. (2007) in the trailing tail. A fresh look at the kinematics of the trailing debris is presented in Koposov et al. (2013), who measure  $\sim 14 \pm 1 \text{ km s}^{-1}$  only a few degrees away from the location where Monaco et al. (2007) obtain  $8.3 \pm 0.9 \text{ km s}^{-1}$ . These two measurements are not consistent with each other at  $> 3\sigma$  level. A possible resolution of this apparent inconsistency can be found in the analysis of Majewski et al. (2013), who discover two distinct stellar populations in the Sgr remnant. According to their Figure 2, there exists a metal-poor sub-population with typical velocity dispersion of  $\sim 14 \text{ km s}^{-1}$  and a metal-rich sub-population with a dispersion of  $\sim 8 \text{ km s}^{-1}$ . Therefore, we hypothesize that a similar stellar population dichotomy might exist in the stream itself. Then, the difference between the dispersion measurements of Monaco et al. (2007) and Koposov et al. (2013) can be explained away if at least one of the spectroscopic samples displayed a strong metallicity bias. A quick look at the Table 5 and the lower panel of Figure 9 in Monaco et al. (2007) reveals that, indeed, their measurements are biased towards the highest metallicity members (M-giant stars) of the trailing tail. This is contrast to the SDSS spectroscopic sample used by Koposov et al. (2013), where the metallicity distribution is substantially broader, encompassing the range between  $[\text{Fe}/\text{H}]=-3$  and  $[\text{Fe}/\text{H}]=-0.5$ .

Encouraged by the detection of multiple stellar populations in the Sgr remnant, we present here an in-depth study of the chemodynamical properties of the Sgr tidal tails. More precisely, we model the spectroscopy of the likely Sgr stream members available as part of SDSS DR9 (Section 2). According to our analysis, across the entire SDSS footprint, stars in both the leading and the trailing tail exhibit a clear dichotomy, in the sense that the more metal-rich population possesses a lower line-of-sight velocity dispersion

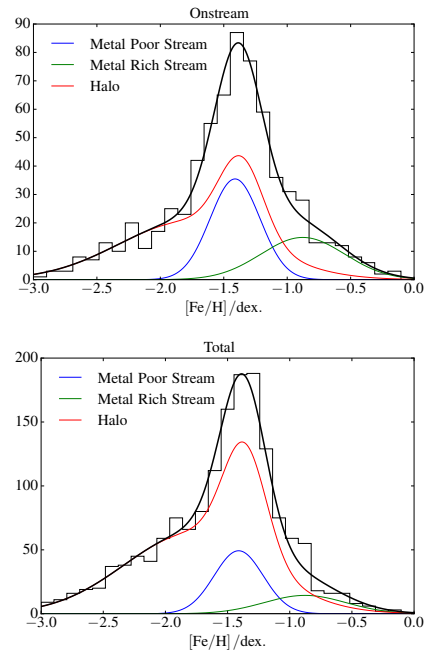


**Figure 4.** As Fig. 3, but for the leading stream stars with  $\tilde{\Lambda}_\odot < 150^\circ$ .

in comparison to the more metal-poor one. Our findings immediately remove any seeming tension between the results of Monaco et al. (2007) and Koposov et al. (2013). Naturally, the presence of a substantially hotter metal-poor population in the stream demands a more massive progenitor than that inferred by Law & Majewski (2010b). The link between the stream dispersion and the progenitor mass can be established through an analysis of an extensive suite of numerical simulations, such that the effects of the dynamical friction are taken into account. Such comprehensive analysis is beyond the scope of this paper. However, to gauge the range of the Sgr progenitor masses allowed by our dispersion measurements, we carry out a series of N-body experiments where two-component Sgr dwarf prototypes are accreted by realistic MW hosts in the presence of dynamical friction (Section 3). The implications of our investigation are reported in Section 4.

## 2 CHEMISTRY AND KINEMATICS OF THE SGR STREAM IN THE SDSS DR9

### 2.1 Spectroscopic Selection

To study the chemistry and the kinematics of the Sagittarius stream we take advantage of the largest spectroscopic dataset to date - the SDSS. More precisely, we use the combination of the SDSS and SEGUE spectroscopic surveys, available in SDSS DR9 (Ahn et al. 2012; Yanny et al. 2009). This consists of medium-resolution spectroscopy of stars covering a large portion of the sky, with many fields overlapping with the leading and trailing arms of the Sagittarius stream. The stellar parameters and metallicities of individual stars were derived through the detailed fitting of synthetic spectra using the SEGUE Stellar Parameter Pipeline (see e.g. Allende Prieto et al. 2008; Lee et al. 2008, 2011; Smolinski et al. 2011).

As a first step, we identify the likely stream member stars by transforming the equatorial Right Ascension and Declination coordinates to the heliocentric stream-aligned positions ( $\tilde{\Lambda}_\odot, \tilde{B}_\odot$ ), as

	$234^\circ < \tilde{\Lambda}_\odot < 248^\circ$	$248^\circ < \tilde{\Lambda}_\odot < 255^\circ$	$255^\circ < \tilde{\Lambda}_\odot < 266^\circ$	$266^\circ < \tilde{\Lambda}_\odot < 274^\circ$
$N_{\text{stars}}$	257	242	228	254
$w_1$	$0.473 \pm_{0.038}^{0.040}$	$0.478 \pm_{0.040}^{0.039}$	$0.429 \pm_{0.040}^{0.040}$	$0.390 \pm_{0.041}^{0.040}$
$w_2$	$0.141 \pm_{0.027}^{0.029}$	$0.156 \pm_{0.028}^{0.030}$	$0.154 \pm_{0.028}^{0.030}$	$0.089 \pm_{0.022}^{0.026}$
$\sigma_1 / \text{km s}^{-1}$	$15.7 \pm_{1.3}^{1.5}$	$13.5 \pm_{1.0}^{1.2}$	$12.5 \pm_{1.0}^{1.2}$	$12.6 \pm_{1.5}^{1.5}$
$\sigma_2 / \text{km s}^{-1}$	$14.0 \pm_{2.6}^{2.7}$	$8.5 \pm_{1.2}^{1.5}$	$7.1 \pm_{1.3}^{1.7}$	$6.4 \pm_{2.6}^{3.8}$
$\sigma_{MW} / \text{km s}^{-1}$	$113.6 \pm_{7.9}^{8.9}$	$114.7 \pm_{8.6}^{9.3}$	$106.8 \pm_{7.0}^{8.1}$	$105.3 \pm_{6.2}^{6.8}$
$\bar{v}_1 / \text{km s}^{-1}$	$-142.5 \pm_{1.9}^{1.9}$	$-124.2 \pm_{1.2}^{1.2}$	$-107.4 \pm_{1.3}^{1.3}$	$-79.0 \pm_{1.5}^{1.5}$
$d\bar{v}_1/d\Lambda / \text{km s}^{-1} \text{ deg.}^{-1}$	$2.24 \pm_{0.37}^{0.36}$	$0.75 \pm_{0.49}^{0.47}$	$2.59 \pm_{0.29}^{0.29}$	$3.53 \pm_{0.53}^{0.54}$
$\bar{v}_2 / \text{km s}^{-1}$	$-143.5 \pm_{4.0}^{3.8}$	$-114.7 \pm_{1.7}^{1.6}$	$-98.6 \pm_{1.5}^{1.5}$	$-75.7 \pm_{2.2}^{1.6}$
$d\bar{v}_2/d\Lambda / \text{km s}^{-1} \text{ deg.}^{-1}$	$3.97 \pm_{0.69}^{0.71}$	$0.30 \pm_{0.64}^{0.63}$	$2.74 \pm_{0.35}^{0.34}$	$1.97 \pm_{0.59}^{0.49}$

**Table 1.** Fitted parameters for the trailing stream, including the number of stars in each bin  $N$ , the weights of the Gaussians  $w_i$ , and the velocity dispersions  $\sigma_i$  around the mean velocity tracks for the metal-rich and metal-poor populations.

	$100^\circ < \tilde{\Lambda}_\odot < 110^\circ$	$110^\circ < \tilde{\Lambda}_\odot < 120^\circ$	$120^\circ < \tilde{\Lambda}_\odot < 130^\circ$	$130^\circ < \tilde{\Lambda}_\odot < 140^\circ$
$N_{\text{stars}}$	347	328	420	455
$w_1$	$0.181 \pm_{0.031}^{0.032}$	$0.143 \pm_{0.028}^{0.030}$	$0.152 \pm_{0.029}^{0.030}$	$0.160 \pm_{0.029}^{0.033}$
$w_2$	$0.088 \pm_{0.020}^{0.023}$	$0.135 \pm_{0.022}^{0.024}$	$0.106 \pm_{0.022}^{0.025}$	$0.121 \pm_{0.027}^{0.027}$
$\sigma_1 / \text{km s}^{-1}$	$31.4 \pm_{5.9}^{7.7}$	$21.6 \pm_{3.5}^{4.5}$	$15.0 \pm_{3.2}^{4.6}$	$16.9 \pm_{3.0}^{3.5}$
$\sigma_2 / \text{km s}^{-1}$	$19.7 \pm_{4.3}^{6.5}$	$12.0 \pm_{1.5}^{1.9}$	$6.0 \pm_{1.4}^{1.9}$	$10.5 \pm_{1.7}^{2.0}$
$\sigma_{MW} / \text{km s}^{-1}$	$110.3 \pm_{4.4}^{4.7}$	$115.7 \pm_{4.5}^{4.9}$	$115.8 \pm_{5.1}^{5.6}$	$127.9 \pm_{5.6}^{6.0}$
$\bar{v}_1 / \text{km s}^{-1}$	$-87.6 \pm_{7.3}^{6.6}$	$-107.2 \pm_{3.9}^{3.8}$	$-110.7 \pm_{3.5}^{3.0}$	$-123.8 \pm_{3.8}^{4.0}$
$d\bar{v}_1/d\Lambda / \text{km s}^{-1} \text{ deg.}^{-1}$	$-2.3 \pm_{1.6}^{1.6}$	$-1.59 \pm_{0.93}^{0.91}$	$0.89 \pm_{0.84}^{0.80}$	$-3.5 \pm_{1.2}^{1.3}$
$\bar{v}_2 / \text{km s}^{-1}$	$-77.5 \pm_{5.9}^{6.2}$	$-90.2 \pm_{2.0}^{1.9}$	$-107.1 \pm_{1.3}^{1.3}$	$-116.7 \pm_{2.6}^{2.5}$
$d\bar{v}_2/d\Lambda / \text{km s}^{-1} \text{ deg.}^{-1}$	$-1.9 \pm_{1.4}^{1.3}$	$-0.65 \pm_{0.54}^{0.50}$	$-2.72 \pm_{0.47}^{0.50}$	$0.79 \pm_{0.74}^{0.70}$

**Table 2.** As Table 1, but for the leading stream.

defined in Majewski et al. (2003). Note that following the convention of Belokurov et al. (2014),  $\tilde{\Lambda}_\odot$  increases in the direction of the Sgr progenitor's motion and  $\tilde{B}_\odot$  points towards the Galactic North Pole. The stream member stars are selected as all spectroscopic targets with  $|\tilde{B}_\odot| \leq 12^\circ$ . To ensure that all targets have robust stellar parameters, a minimum signal-to-noise ratio of 25 is enforced. Finally, following de Boer et al. (2015), we further refine the selection by choosing the spectroscopically confirmed giants. These are selected as stars with  $\log g \leq 3.5$  and  $4300 \leq T_{\text{eff}} \leq 6000\text{K}$ . The combination of the selection criteria described above yields  $\sim 9,000$  stars in total.

Fig. 1 shows the distribution of the selected stars in the plane of the radial velocity (corrected for the Solar reflex motion)  $v_{\text{GSR}}$  and the Sgr stream longitude  $\tilde{\Lambda}_\odot$  (left panel). Clearly, even with the above cuts in place, the effect of the Galactic contamination is still appreciable, especially for the leading stream in the North. The foreground populations come from both the nearby halo, as evidenced by the large velocity dispersion across the whole range of  $\tilde{\Lambda}_\odot$ , as well as the thick disk as revealed by a portion of stars following a narrow velocity track at low Galactic latitudes (e.g.  $150^\circ < \tilde{\Lambda}_\odot < 230^\circ$ ). To reduce the foreground presence, we utilize the fact that the stream in these parts of the sky is at a much greater distance, i.e. ( $> 15 \text{ kpc}$ ) than the bulk of the Milky Way disk and halo stars (Belokurov et al. 2014). Therefore, we proceed as follows. We derive distances for the stars in our sample by placing them on the PARSEC isochrones (Bressan et al. 2012). The isochrone's metallicity and surface gravity are chosen according to the star's metallicity  $[\text{Fe}/\text{H}]$  and surface gravity  $\log g$  derived from

spectroscopy, while the age is kept constant at  $8 \times 10^9$  yr. With these assumptions, the stellar absolute magnitudes are determined in the  $g$ ,  $r$ ,  $i$  and  $z$  bands. The median of the four absolute magnitude estimates is taken as our measured distance. Accordingly, all stars with a derived distance in excess of  $15 \text{ kpc}$  are removed from the sample. This approach is similar in spirit to the de-contamination procedure employed by de Boer et al. (2015), though differing in detail.

The final (cleaned) selection of  $\sim 4,300$  stars is shown in the middle panel of Fig. 1. For comparison, the stars rejected by the distance cut are displayed in the right panel of the Figure. Reassuringly, it can be seen that the method substantially reduces the contamination from the Milky Way disk+halo whilst leaving the stream signal intact. In fact, it appears that the majority of the remaining MW population is that of the halo, as no clear velocity gradient is visible - other than that of the Sgr stream itself - in the middle panel of the Figure. Note that, even after the substantial cleaning of the sample, the leading tail, i.e. stars with  $\tilde{\Lambda}_\odot < 200^\circ$  appears to be more affected by the Galactic contamination as compared to the trailing debris, i.e. stars with  $\tilde{\Lambda}_\odot > 200^\circ$ .

## 2.2 Metallicity Distribution Function of the Galactic halo and the Sgr Stream

Before the behaviour of the stream can be studied in the space of metallicity and velocity, a model for the distribution of the Milky Way stars must be established. To this end, we empirically determine the metallicity distribution function (MDF) of the Milky Way

contaminant population by selecting all stars satisfying the criteria described in Section 2.1, but with  $|\tilde{B}_\odot| \geq 15^\circ$  to exclude the majority of stream members. The MDF returned by this selection is displayed as a histogram in Fig. 2. We find that this metallicity distribution can be represented adequately with a mixture of two Gaussians (individual components shown as dashed lines, and their sum as a solid line). Of course, this distribution is obviously not the *true* underlying MDF of the Milky Way halo – but is, instead, the distribution modulated by the SEGUE selection function. The two Gaussians in our model (determined through maximum likelihood analysis of the SDSS spectra) have the following centers and widths:  $(\mu_{MW1}^{[Fe/H]}, \sigma_{MW1}^{[Fe/H]}) = (-1.38, 0.15)$  dex and  $(\mu_{MW2}^{[Fe/H]}, \sigma_{MW2}^{[Fe/H]}) = (-1.81, 0.56)$  dex. Even while affected by the selection bias, this blend of a narrow metal-rich ingredient and a broad metal-poor is not inconsistent with the chemical properties of the Galactic halo in the literature (see e.g. Helmi 2008; Beers et al. 2012; Fernández-Alvar et al. 2015).

To measure the MDF of the stream we exploit the fact that it displays a clear trend in velocity  $v_{\text{GSR}}$  as a function of  $\tilde{\Lambda}_\odot$  longitude. To boost the stream signal and to minimize the Milky Way contamination, we select stars with velocities within  $\pm 45 \text{ km s}^{-1}$  from the mean stream track in  $v_{\text{GSR}}$  space, as determined in Belokurov et al. (2014). The half-width of the selection region in the phase space corresponds to approximately  $\pm 3\sigma$  of the velocity dispersion found in Koposov et al. (2013). Fig. 3 shows the MDF for the trailing tail, represented by the Sgr candidate stars with  $234^\circ < \tilde{\Lambda}_\odot < 270^\circ$ . The top panel displays only stars within the velocity range of the mean track of the stream, while the bottom panel includes all stars in this range of  $\tilde{\Lambda}_\odot$ . As expected, the only difference between the two panels is the relative scaling of the stream and the halo.

The metallicity distribution displayed in Figure 3 is markedly bi-modal, thus indicating two distinct populations of stars in the stream. Motivated by this discovery, we model the distribution with a mixture of the contaminant MW MDF and two additional Sgr trailing (ST) Gaussians with  $(\mu_{\text{ST1}}^{[Fe/H]}, \sigma_{\text{ST1}}^{[Fe/H]}) = (-1.33, 0.27)$  and  $(\mu_{\text{ST2}}^{[Fe/H]}, \sigma_{\text{ST2}}^{[Fe/H]}) = (-0.74, 0.18)$  dex. Compared to the halo overall, the stream lacks a substantial metal-poor component. Instead, there is a conspicuous metal-rich population, in agreement with a multitude of previous studies of both the remnant and the stream (see e.g. Sbordone et al. 2007; Yanny et al. 2009; Chou et al. 2010; Koposov et al. 2013; de Boer et al. 2014, 2015).

Similarly, Fig. 4 presents the MDF of the leading tail, i.e. the portion of the stream with  $\tilde{\Lambda}_\odot < 150^\circ$ . Here, the metal-rich sub-population is less obvious compared to the trailing stream. Through a maximum-likelihood analysis, we find that a combination of these two Gaussians describe the Sgr leading (SL) MDF well:  $(\mu_{\text{SL1}}^{[Fe/H]}, \sigma_{\text{SL1}}^{[Fe/H]}) = (-1.39, 0.22)$  and  $(\mu_{\text{SL2}}^{[Fe/H]}, \sigma_{\text{SL2}}^{[Fe/H]}) = (-1.00, 0.34)$ . In the leading tail MDF, the centres of the metallicity distributions of the two sub-populations are closer to each other, with a more significant overlap as compared to those in the trailing tail. Also, note that the metal-rich component of the MW foreground model is coincident with the metal-poor sub-population of the Sgr leading tail.

These differences and similarities between the MDFs of the two tails and the MW halo reflect various astrophysical and observational effects at play. To begin with, there exists a known metallicity gradient along the Sgr stream, and the regions probed by our analysis in the leading and the trailing tails are offset from the progenitor by different amounts. More important, perhaps, are the selection biases inherent to the SDSS spectroscopic sample. Finally,

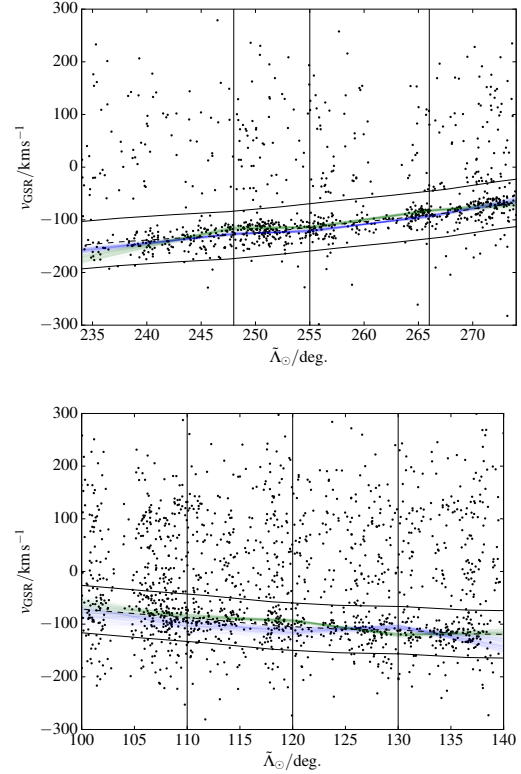


**Figure 5.** Model mean velocity track and bin walls for the trailing (upper panel) and leading (lower panel) streams. The solid vertical lines indicate the bin walls, the dashed black lines show the mean velocity of the track from Belokurov et al. (2014). The solid black lines show the region in velocity space used for selecting stream stars to determine the stream’s MDF components. Finally, the blue and green lines show 100 samples of the mean velocity track from the posterior of our chemo-dynamical modelling for the low and high metallicity populations.

the simplicity of our decomposition of the Sgr MDF into individual components should not be understated. Nonetheless, we believe that, to first approximation, the model described below attempts to account for possible MDF variations caused by the three factors described above, as it allows the relative contribution of each sub-population to change from bin to bin in  $\tilde{\Lambda}_\odot$ .

### 2.3 A Link between Chemistry and Kinematics

With the metallicity components of the stream in hand, we are now able to link the stream chemistry with the kinematics. Namely, we strive to determine the mean velocity and its dispersion for each of the two metallicity sub-populations along the stream. We model the chemistry and kinematics in 4 individual bins of  $\tilde{\Lambda}_\odot$  for both trailing and leading tails. We choose the bin boundaries as follows:  $(234^\circ, 248^\circ)$ ,  $(248^\circ, 255^\circ)$ ,  $(255^\circ, 266^\circ)$ ,  $(266^\circ, 274^\circ)$  for trailing, and  $(100^\circ, 110^\circ)$ ,  $(110^\circ, 120^\circ)$ ,  $(120^\circ, 130^\circ)$  and  $(130^\circ, 140^\circ)$  for leading. Note that the trailing tail bin sizes are slightly different from one another to ensure that a similar number of stars are contained in each bin. We model the velocity centroid of each sub-population of each tail independently. We assume that the mean velocity track of each component is well-represented by a piecewise linear function. Within each bin of  $\tilde{\Lambda}_\odot$ , we assume that the velocity distribution of the  $j$ -th sub-population about the linear

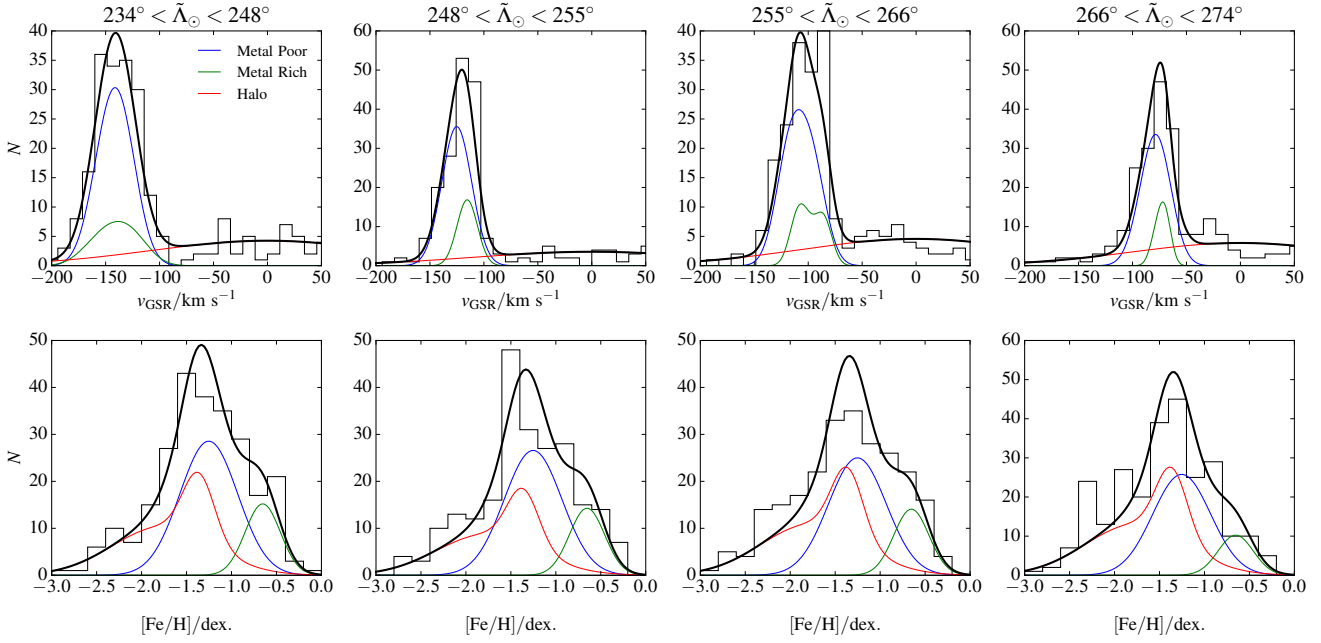


**Figure 6.** The best fitting components of the model in velocity (top row) and metallicity space (bottom row) for the trailing stream. The blue and green lines shows the inferred distributions of low and high metallicity stream components. The red lines display the halo component.

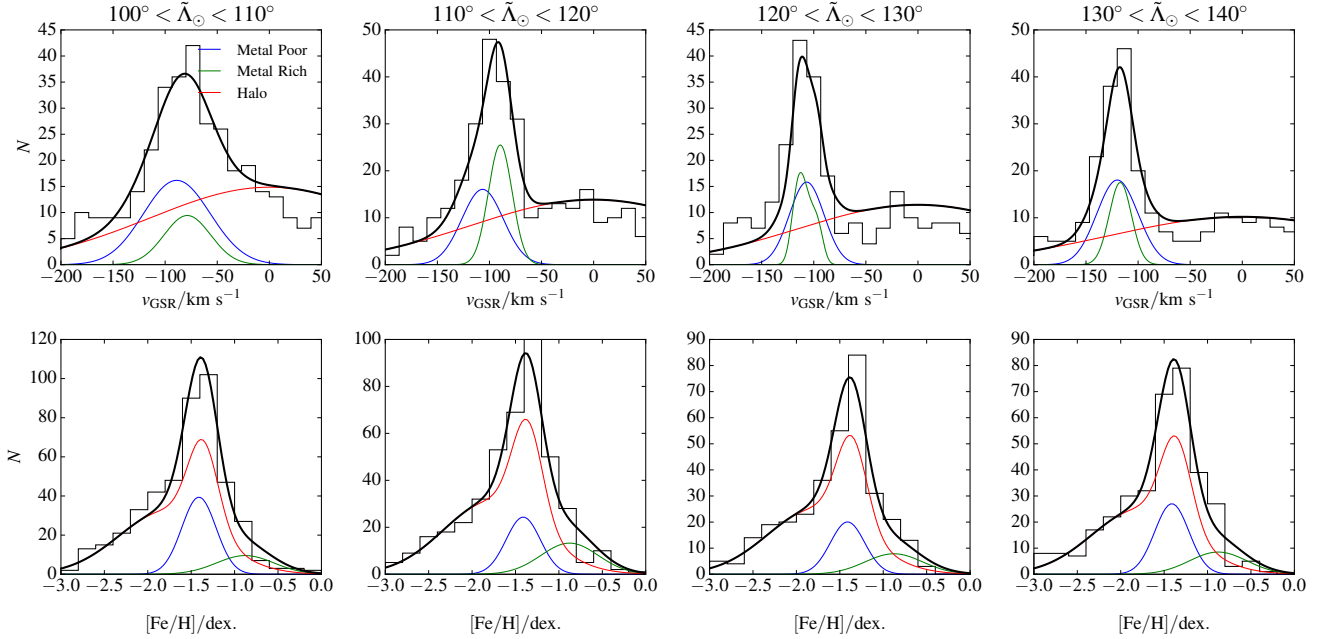


**Figure 7.** As Fig. 6, but for the leading arm.

trend is Gaussian, with a mean  $\mu_j^v$  and a dispersion  $\sigma_j^v$ . Additionally, we assume that the contaminant population has a zero mean velocity and a dispersion of  $\sigma_{\text{MW}}^v$  km s<sup>-1</sup>. Thus, within each bin of  $\tilde{\Lambda}_\odot$ , the likelihood of observing the  $i$ -th star with velocity  $v_{\text{GSR},i}$  and metallicity  $[\text{Fe}/\text{H}]_i$  is simply:

$$\mathcal{L}_i = \sum_{j=1}^3 \frac{w_j P_j([\text{Fe}/\text{H}]_i)}{\sqrt{2\pi[(\sigma_j^v)^2 + (\sigma_i^v)^2]}} \exp\left(-\frac{[v_{\text{GSR},i} - \mu_j^v(\tilde{\Lambda}_\odot)]^2}{2[(\sigma_j^v)^2 + (\sigma_i^v)^2]}\right) \quad (1)$$

Here,  $\sigma_i^v$  is the radial velocity error of  $i$ -th star,  $P_j([\text{Fe}/\text{H}]_i)$  is the probability of observing a star with metallicity  $[\text{Fe}/\text{H}]_i$  belonging to the  $j$ -th sub-population. This probability is Gaussian whose position and shape is fixed by the coefficients determined in the previous sub-section. To clarify, the index  $j$  runs from 1 to 3, corresponding to the two stream and one foreground components. More specifically,  $j = 1$  labels the metal-poor,  $j = 2$  the metal-rich sub-

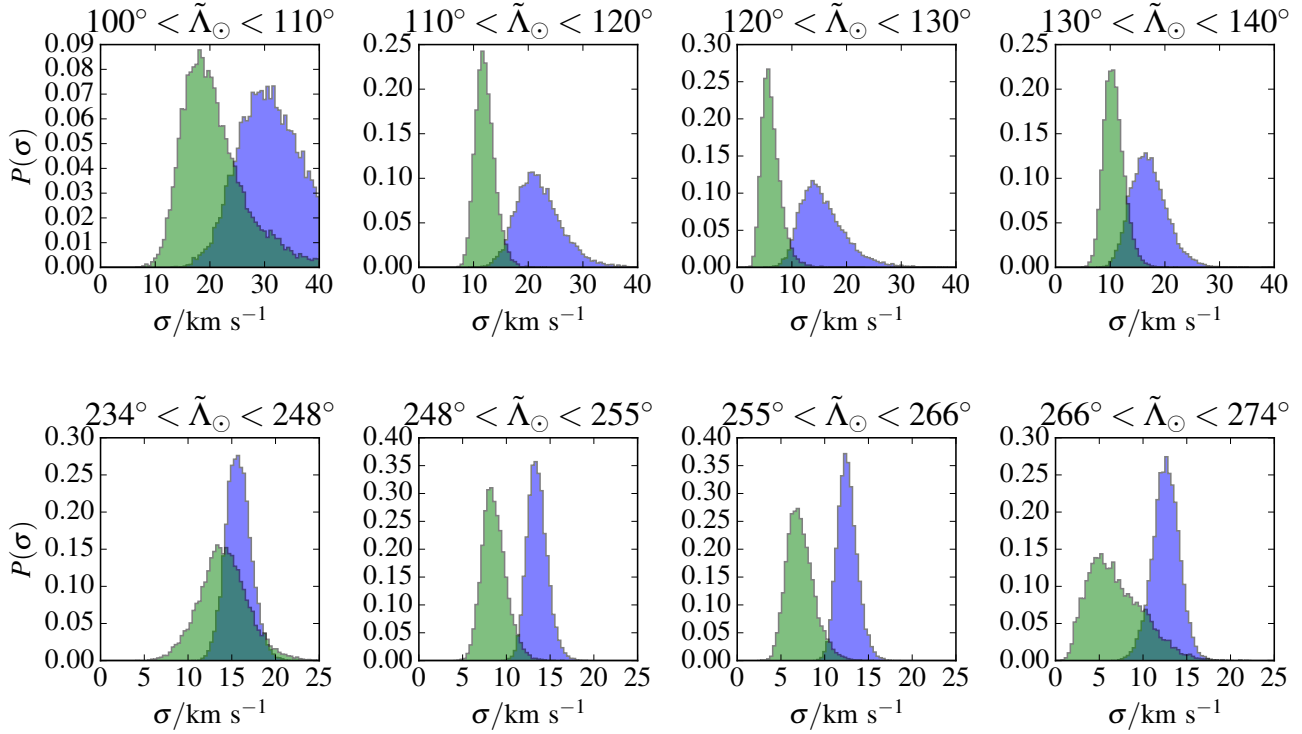


**Figure 8.** The posterior probability distributions for the velocity dispersions of the low metallicity (blue) and high metallicity (green) components of the leading (upper row) and trailing (bottom row) stream. The low metallicity stars show a significantly enhanced velocity dispersion, compared with the high metallicity stars. Additionally the leading stream shows a systematically higher line of sight velocity dispersion compared to the trailing stream.

populations, while  $j = 3$  labels the MW. We enforce that sum of the relative weights equals to 1, i.e.  $w_j = 1$ . In total, for each tail we have 30 independent free parameters encompassing 4 bins in  $\tilde{\Lambda}_\odot$ : 8 weights, 12 velocity dispersions and 10 mean stream velocities at 5 bin walls. All of the kinematic parameters are constrained simultaneously. The results of the fit are presented in Tables 1 and 2 for the trailing and leading tails respectively.

Fig. 5 shows the behaviour of the mean of the velocity of the trailing and leading tails correspondingly as a function of  $\tilde{\Lambda}_\odot$ . The model prediction for the stream’s metal-poor component is shown in blue, and for the metal-rich in green. The differences between the velocity tracks of the two sub-populations are typically rather small, of order of  $10 \text{ km s}^{-1}$ . Note, however, that even such a small velocity mismatch could be enough to inflate the velocity dispersion if it was assumed to be the same for all stream members indiscriminately.

Figs 6 and 7 give a detailed view of the velocity (top row) and the metallicity (bottom row) distributions in each  $\tilde{\Lambda}_\odot$  bin in the trailing and leading tails correspondingly. As before, black histograms are the data, and the blue (green) curves show models for the metal-poor (metal-rich) sub-populations. Finally, the red line displays our model for the MW halo contribution. As is evident from the Figures, the observed velocity and metallicity distributions are reproduced adequately. This is helped by the fact that both in the North and the South, the Sgr stream stands out kinematically from the bulk of the Galactic foreground. While the gross features of the distributions are never amiss, some of the finer details are clearly not captured by our model. This is hardly surprising though, as we have postulated that the MW halo can be represented with only one Gaussian component in velocity (although its width is allowed to

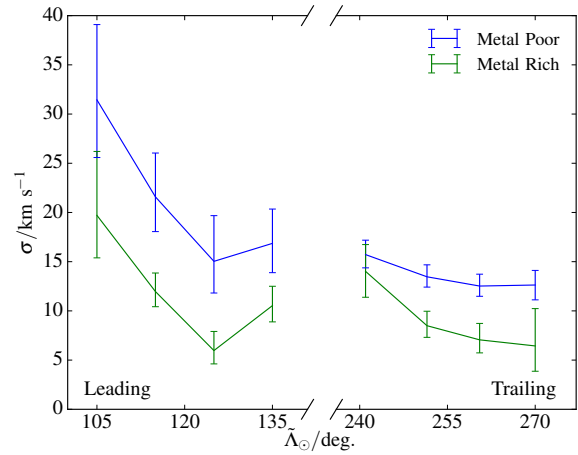


**Figure 9.** Variation of the velocity dispersions in the metal-rich and metal-poor components as a function of the Sgr stream longitude for both leading and trailing stream.

vary from bin to bin), and a combination of two broad Gaussians in metallicity. However, it is likely that there exists unmixed - and thus probably highly peaked in terms of their MDF and phase-space distribution - stellar halo sub-structures in the areas of the sky under consideration. Generally, these would include portions of unrelaxed stellar debris similar to those detected by Schlafman et al. (2009); Starkenburg et al. (2009); Deason et al. (2011); Torrealba et al. (2015); Janesh et al. (2016). Additionally, there exist large



known structures overlapping with the leading tail in the North, such as the Virgo Cloud (see e.g. Duffau et al. 2006; Newberg et al. 2007; Martínez-Delgado et al. 2007; Jurić et al. 2008); and the trailing tail in the South, such as the Cetus stream (Newberg et al. 2009; Koposov et al. 2012).

According to Fig. 6 and Table 1, the trailing tail data in the South suffers very little MW foreground contamination. The stream runs across the four  $\tilde{\Lambda}_\odot$  bins with substantial negative velocity. Typically, in each bin approximately half of the stars in our final sample belongs to the Sgr stream with  $\sim 70\%$  in the metal-poor sub-population and  $\sim 30\%$  in metal-rich. The other half of the sample resides in the MW component, for which we estimate the velocity dispersion to be in the range  $100\text{kms}^{-1} < \sigma_{\text{MW}}^v < 115\text{kms}^{-1}$ . A striking result of the modelling is the substantial difference between the kinematical properties of the two Sgr stream sub-populations split by metallicity. As mentioned before, there exists a  $\sim 10\text{ km s}^{-1}$  offset between their mean velocities. More intriguingly, the sub-populations appear to have rather different velocity dispersions. The metal-rich sub-population exhibits kinematics well approximated by a Gaussian with  $\sigma_{\text{ST2}}^v \sim 8\text{ km s}^{-1}$ . This is in good agreement with the value reported by Monaco et al. (2007) using high resolution spectroscopy of (mostly) M-giant stars in the neighbouring part of the sky. The metal-poor component is almost twice as hot, with  $\sigma_{\text{ST2}}^v \sim 13\text{ km s}^{-1}$ , in consensus with the measurements of Koposov et al. (2013) who also used the SDSS spectra in their analysis, albeit without distinguishing between the two metallicity populations.

Fig. 7 and Table 2 present the results of the leading tail modeling. In the North, the Sgr stream constitutes only 25% of the (cleaned) spectroscopic sample, with the two metallicity sub-populations contributing almost equal amounts:  $\sim 60\%$  is metal-poor and  $\sim 40\%$  is metal-rich. Note, however, that as described above, the actual definitions of the “metal-rich” and “metal-poor” are now different compared to the trailing tail data. Interestingly, we find a slightly hotter MW halo, with the velocity dispersion in the range  $110\text{kms}^{-1} < \sigma_{\text{MW}}^v < 130\text{kms}^{-1}$ . The dispersion of the Sgr stream itself is also inflated: we find  $15\text{kms}^{-1} < \sigma_{\text{SL1}}^v < 30\text{kms}^{-1}$  for the metal-poor sub-population, and  $6\text{kms}^{-1} < \sigma_{\text{SL2}}^v < 20\text{kms}^{-1}$  for the metal-rich.

Fig. 8 displays the posterior distributions for the Sgr stream velocity dispersion in both leading and trailing tails in each bin of  $\tilde{\Lambda}_\odot$  studied. In all bins and in both tails, the picture remains unchanged: the metal-poor sub-population exhibits an enhanced velocity dispersion compared to the metal-rich one. While in all cases there is a noticeable overlap between the posterior distributions, their peaks are typically  $2\sigma$  apart. Figure 9 summarizes the velocity dispersion behaviour as a function of  $\tilde{\Lambda}_\odot$ . There appears to be a clear evolution of the dispersion with the stream longitude in both the leading and the trailing tails: the dispersion increases towards lower  $\tilde{\Lambda}_\odot$ .

Some of the change in the line-of-sight velocity dispersion of the debris along the stream is likely due to the projection effects. For different  $\tilde{\Lambda}_\odot$ , the line of sight from the heliocentric observer pierces the stream at different angles. Therefore, the dispersion is expected to be higher for directions where the angle between the line of sight and the debris orbital velocity is smaller. For the trailing tail, this occurs around  $\tilde{\Lambda}_\odot \sim 240^\circ$ . Additionally, the intrinsic velocity dispersion of the stars in the stream is expected to grow due to the debris evolution in the gravitational potential. In the simplest case, in a spherical potential, the stream’s cross-section and velocity dispersion in the radial direction will tend to inflate due to differential apsidal precession (see e.g. Johnston et al. 2001; Hendel &

Johnston 2015). Moreover, as shown in simulations of the Sgr disruption (see e.g. Law & Majewski 2010b; Gibbons et al. 2014), the stream separates into individual streamlets, consisting of the debris unbound during subsequent pericentric passages (see also Amorisco 2015). With time, these “feathers” will misalign – also due to the differential apsidal precession – making the stream appear ruffled around the apogalacticon, and thus contributing to the line-of-sight velocity dispersion increase. As measured by Belokurov et al. (2014), the leading tail apocenter lies around  $\tilde{\Lambda}_\odot \sim 70^\circ$ , hence some of the dispersion rump-up around  $\tilde{\Lambda}_\odot \sim 100^\circ$  could be due to the superposition of stars stripped at different epochs. Finally, in a flattened potential, the differential orbital plane precession will lead to the debris fanning in the direction perpendicular to the stream plane, therefore also inflating the line-of-sight velocity dispersion (see e.g. Erkal et al. 2016). As pointed out by these authors, the amount of debris fanning varies strongly with the angle along the stream.

### 3 FROM DWARF TO STREAM

Clearly, the debris velocity dispersion of  $\sim 15\text{kms}^{-1}$  must imply a progenitor more massive than  $\sim 10^9 M_\odot$  as inferred from the measurement of  $8\text{kms}^{-1}$ . However, the link between the progenitor’s original mass and the final velocity dispersion in the stream is quite labyrinthine. First, rather than the dispersion of the stripped DM particles, we are interested in the kinematics of the *stellar* debris, whose properties will depend on how deeply embedded the progenitor’s stellar component is within the parent DM halo. Second, the progenitor’s velocity dispersion will evolve during the disruption due to mass loss, which will be reflected in the kinematics of the tails. Importantly, the mass loss rate depends on the orbit of the progenitor, which will be affected by dynamical friction. Finally, the direct comparison to the data is only possible if the stream’s 3D geometry matches that of the observed stream – otherwise projection effects might bias the inference.

In an attempt to address all of the factors mentioned above, we have settled on the following setup for the Sgr accretion simulation. We explore the behaviour of streams produced through tidal stripping of progenitors of different masses. For each mass, we use three different (massless) stellar components with different sizes. We start our simulations in live DM halos to facilitate accurate modelling of dynamical friction. Once the bulk of the mass is tidally stripped, and the orbits have largely finished their evolution, we move the remaining bound particles into the Law & Majewski (2010b) (parameterized) potential. The last step ensures that the geometry of the simulated tails is correct and we do not need to worry about the projection effects.

#### 3.1 The Progenitor Model

In our model, the dark halo of the Sgr progenitor follows a NFW (Navarro et al. 1996) profile with a density given by

$$\rho_{\text{NFW}} = \frac{M_{200}}{4\pi r_s^2} \frac{(r/r_s)^{-1}(1+r/r_s)^{-2}}{\log(1+c_{200}) - c_{200}/(1+c_{200})} \quad (2)$$

where  $r_s$  is a scale radius,  $M_{200}$  is the mass contained within a radius,  $r_{200}$  where the density of the halo is 200 times the critical density of the universe and  $c \equiv r_{200}/r_s$  is the NFW concentration parameter. To reduce the parameter space through which we need



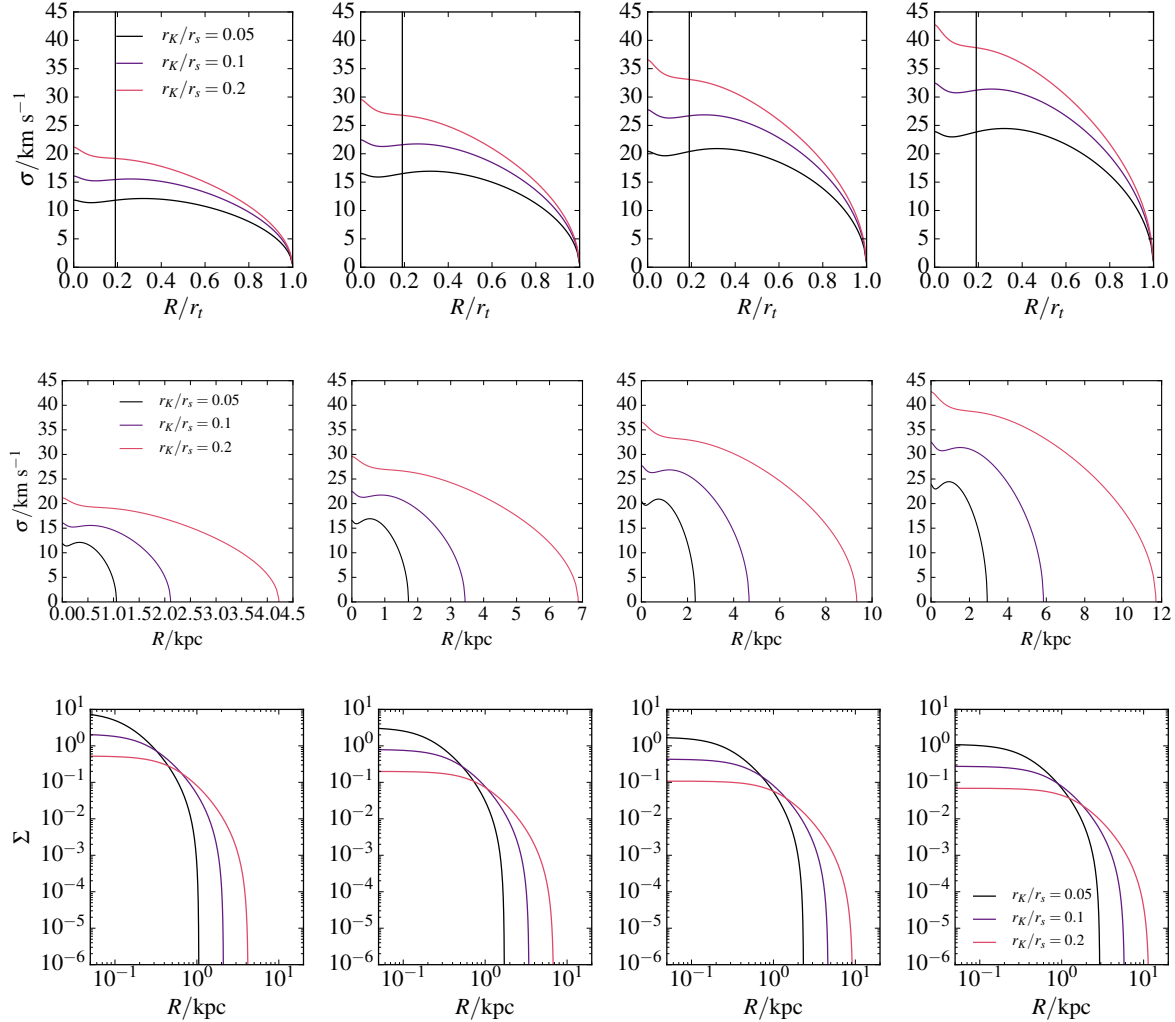


**Figure 10.** *Top and Middle:* the initial projected velocity dispersions for each of the progenitor models, with the top row showing distances in units of tidal radius  $r_t$  and the middle row in kpc. The panels from left to right show the four progenitor masses that we consider,  $1 \times 10^{10} M_\odot$  to  $1 \times 10^{11} M_\odot$  and each of the coloured lines correspond to the degree of embeddedness ( $r_K/r_s$ ) of the stellar particles within each halo. The vertical black line indicates the half light radius. Note that the King model embedded within an NFW halo produces velocity dispersion profiles that are flat out to almost the tidal radius. *Bottom:* initial surface brightness profiles in the simulated Sgr dwarf progenitors. The overall range of half-light radii probed by the 12 models is from 0.2 kpc to 2.2 kpc.

to search, and to ensure that the parameters of our progenitor’s halos are well motivated cosmologically, we link the masses and concentrations of the progenitors halo through the mass-concentration relation of Macciò et al. (2007). The NFW profile of eq. (2) has an infinite mass. To allow us to set up equilibrium realisations, we exponentially truncate the dark halo’s density at the virial radius following the prescription of Kazantzidis et al. (2004).

The stellar component follows a King (1962) profile, with mass density

$$\rho_K = \frac{K}{x^2} \left[ \frac{\arccos(x)}{x} - \sqrt{1-x^2} \right]; \quad x \equiv \left[ \frac{1 + (r/r_K)^2}{1 + (r_t/r_K)^2} \right]^{1/2} \quad (3)$$

where  $r_t$  is the tidal radius,  $r_K$  is a scale radius and  $K$  is an arbitrary constant. In all of our simulations, we choose to keep the ratio  $r_K/r_t$  to be fixed at 8, in keeping with the fits of Majewski et al. (2003) to the light profile of the Sgr dwarf at the present day. We vary the degree of ‘embeddedness’ of the light profile in the

dwarf, described by the ratio  $r_K/r_s$ , choosing values in the range 0.05 – 0.2. These choices yield projected velocity dispersion profiles for the stellar component that are flat out to a few half-light radii. This is shown in the upper panels of Fig. 10, in which the half-light radius is marked by a vertical line. If the Sgr progenitor was a dSph, this is a natural assumption to make. The pioneering work of Kleyana et al. (2002) on Draco provided the first evidence of extended flat velocity dispersion profiles, and this was confirmed by the extensive study of Walker et al. (2007). Recent modelling of dwarf spheroidals also lays emphasis on the very flat dispersion profiles within the radii probed by existing observations (Amorisco & Evans 2011; Burkert 2015). Hence, as Fig. 10 confirms, our progenitor looks very much like a dSph in terms of both its photometric and kinematic properties.

The velocity distribution for the luminous King component and the dark halo is obtained assuming isotropy and using the Ed-

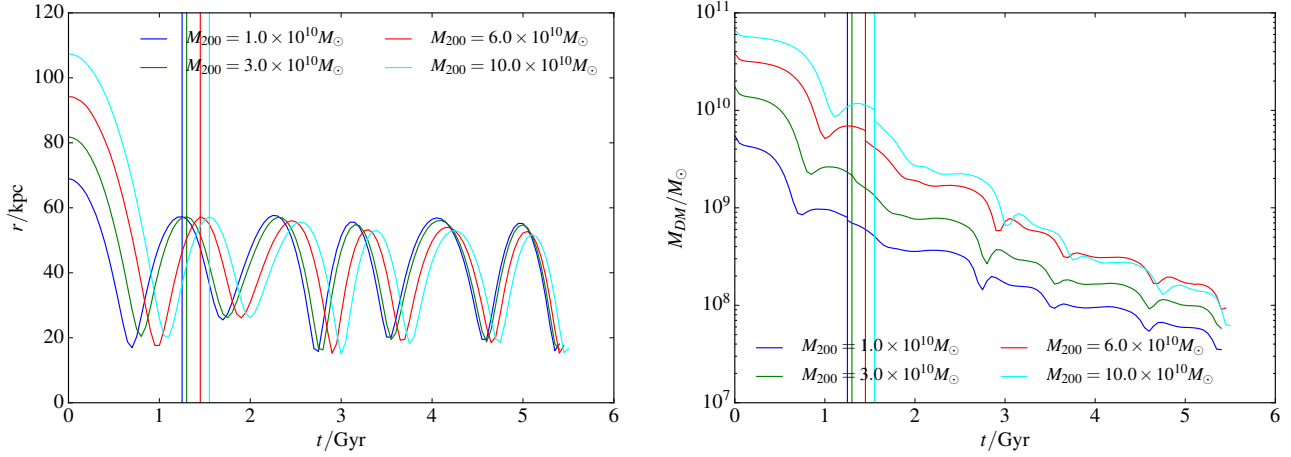


**Figure 11.** The orbit of Sgr (left) and the evolution of the DM mass within the tidal radius (right). The more massive the progenitor, the more effective dynamical friction is at reducing its orbit. The more massive the progenitor, the more ruthless the stripping so that all four models yield a present-day remnant with dark matter mass  $\lesssim 10^8 M_\odot$ .

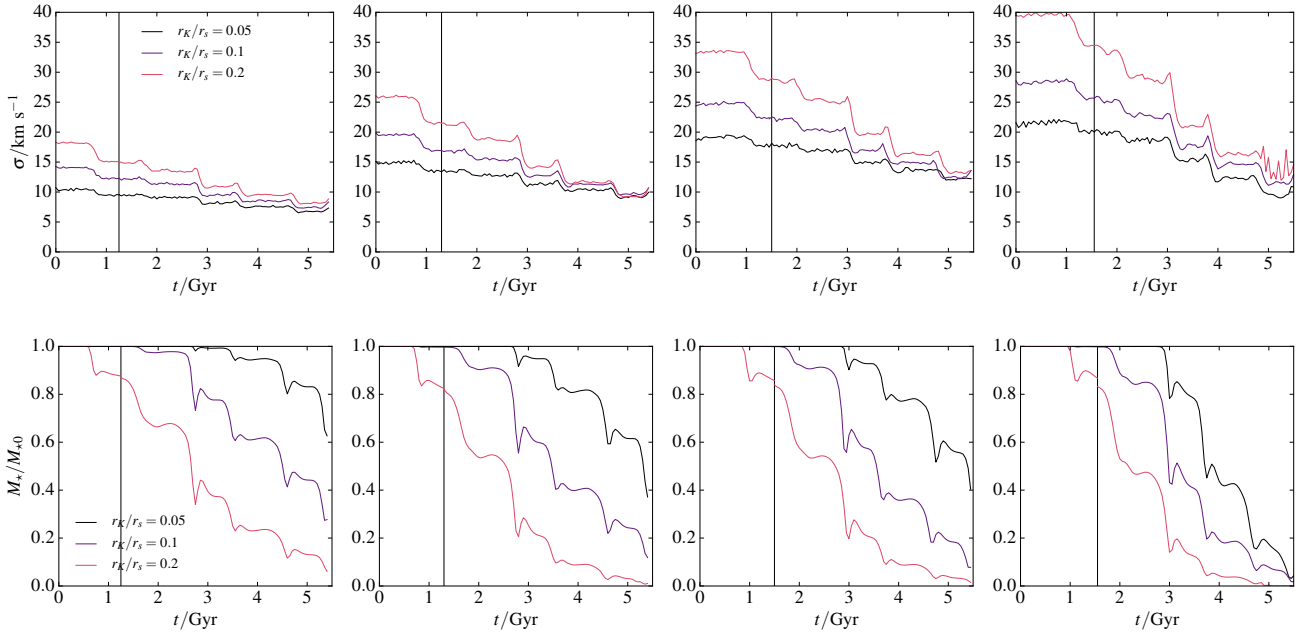


**Figure 12.** Evolution of the velocity dispersion and stellar mass. The vertical black line indicates the crossover from the TF potential to the Law & Majewski (2010b) potential. The panels from left to right show the four progenitor masses that we consider, from  $1 \times 10^{10} M_\odot$  to  $1 \times 10^{11} M_\odot$ . The coloured lines show different embeddedness  $r_K/r_s$  of the stellar distribution. Note that based on the current observations of the stream and the remnant, the Sgr is estimated to have lost  $\sim 50\%$  of its stellar mass. While this could easily be the upper bound, we point out that some of our models have ended up losing more stars than have been observed so far.

dington’s formula (Binney & Tremaine 2008), namely

$$f_i(\epsilon) = \frac{1}{\sqrt{8\pi^2}} \int_0^\epsilon \frac{d^2 \rho_i}{d\Psi^2} \frac{d\Psi}{\sqrt{\epsilon - \Psi}} \quad (4)$$

Here,  $\epsilon$  is the binding energy and  $\Psi$  the potential, which is taken as that of the NFW dark halo only, as it dominates the luminous component. Here,  $i$  refers to either the King or the NFW densities in eqs. (2) or (3).

### 3.2 The Milky Way Models

The Milky Way is modelled in two ways. For the final 4 Gyr of its orbit, the disrupting Sgr is evolved in the Law & Majewski (2010b) potential. Although the details of this potential may not be correct, it has been shown to provide a good match to much of the data on the Sgr stream. The potential is conventional in its choice of disk and bulge, using a Miyamoto & Nagai disk and Hernquist sphere respectively. Unusually, though, the dark halo is misaligned, triax-

ial and logarithmic of form

$$\Psi = -v_0^2 \log (C_1 x^2 + C_2 y^2 + C_3 xy + z^2/q^2 + r_{\text{halo}}^2). \quad (5)$$

The choice of parameters  $C_i$ ,  $q$  and  $r_{\text{halo}}$  yields a triaxial dark matter halo whose minor to major axis ratio  $(c/a)_\Phi = 0.72$  and intermediate to major axis ratio  $(b/a)_\Phi = 0.99$  at radii  $20 \text{ kpc} < r < 60 \text{ kpc}$ , with the minor, intermediate and major axes of this halo lie along the directions  $(\ell, b) = (7^\circ, 0^\circ)$ ,  $(0^\circ, 90^\circ)$  and  $(97^\circ, 0^\circ)$  respectively.

For the initial phase of the simulation, where the Sgr dwarf falls into the Milky Way, we represent the potential using a live realisation of the ‘‘truncated flat rotation curve’’ (TF) models presented in Gibbons et al. (2014). These are a three parameter family of models representing the total matter content of the galaxy, with a rotation curve that is flat, with amplitude  $v_0$  in their inner part, which then smoothly transitions at a scale radius  $r_{\text{tf}}$  into a power law decline in their outer parts with slope  $\alpha$ . The rotation curves of these models have the form

$$v_c^2 = \frac{v_0^2 r_{\text{tf}}^\alpha}{(r_{\text{tf}}^2 + r^2)^{\alpha/2}} \quad (6)$$

which implies a density

$$\rho_{\text{TF}} = \frac{v_0^2}{4\pi G} \frac{1 - (\alpha - 1)(r/r_{\text{tf}})^2}{r^2[(r/r_{\text{tf}})^2 + 1]^{\alpha/2+1}} \quad (7)$$

We choose the parameters  $v_0 = 230 \text{ km s}^{-1}$ ,  $r_{\text{tf}} = 15 \text{ kpc}$  and  $\alpha = 0.5$  corresponding to the most likely solution from Gibbons et al. (2014).

In this form, the TF model has a divergent mass for  $\alpha < 1$ . To be able to construct an equilibrium realization of this density, we must truncate it. We do this by exponentially truncating the density at a radius  $r_{\text{tr}}$ , with a decay scale of  $r_{\text{d}}$ , whilst ensuring that the resulting density has a continuous logarithmic derivative. The modified density is then

$$\rho_{\text{TF, trunc}} = \begin{cases} \rho_{\text{TF}}(r) & r < r_{\text{tr}}, \\ \rho_{\text{TF}}(r) \left(\frac{r}{r_{\text{tr}}}\right)^{r_{\text{tr}}/r_{\text{d}}} \exp\left(-\frac{r-r_{\text{tr}}}{r_{\text{d}}}\right) & r > r_{\text{tr}}. \end{cases} \quad (8)$$

To ensure that this truncation procedure has a negligible effect on the velocity dispersion of the resulting halo, we choose the truncation radius to be much larger than the initial apocentre of the largest Sgr orbit that we consider, setting  $r_{\text{tr}} = 500 \text{ kpc}$  and  $r_{\text{d}} = 15 \text{ kpc}$ . The distribution function for this model is then found by using the Eddington formula (4). Following the example of Kazantzidis et al. (2004), the  $d^2\rho/d\psi^2$  term can be evaluated easily in terms of derivatives of the density with respect to  $r$  (which are available analytically), and expression involving  $d\psi/dr$  and  $d^2\psi/dr^2$ . These terms can be expressed in terms of the enclosed mass  $M(r)$  and the density. Thus, the integral in Eddington’s formula reduces to a simple numerical quadrature.

### 3.3 Evolution of the 2-component Sgr model

The simulation proceeds in 2 phases. First, we evolve the Sgr in the TF potential until a Crossover Point where most of its DM halo is stripped and the stellar components begins to disrupt. By the time the Sgr gets to the Crossover Point, it has lost between 90% and 99% of its dark matter mass. Most of the orbital evolution happens during this time. At the Crossover Point, we take all the bound particles, (i.e. particles within the tidal radius of

Sgr) and place them into the Law & Majewski (2010b) potential and evolve for 4 Gyr. At the end of the simulation, the progenitor is near the current Sgr location and the tidal tails look as they should. The location of this Crossover Point is fixed by integrating the orbit of Sgr from its current position back by 4 Gyr. At this point, Sgr is at  $(X, Y, Z) = (-48, -22, -21) \text{ kpc}$  and  $(V_X, V_Y, V_Z) = (39, -6, -83) \text{ km s}^{-1}$  where  $(X, Y, Z)$  is a right-handed Cartesian set with the  $X$  axis pointing towards the Sun.

To match at the Crossover Point, we proceed as follows. We integrate the Sgr back in time from Crossover for 1 orbital period with an approximate prescription for the dynamical friction. Chandrasekhar (1960) provided such a formula under the idealized assumption of an undisruptable stellar system moving through a homogeneous background of stars with a Maxwellian velocity distribution, namely

$$\frac{d\mathbf{v}}{dt} = -\frac{4\pi G^2 M \rho \ln \Lambda}{v^2} \left[ \text{erf}(X) - \frac{2X}{\sqrt{\pi}} e^{-X^2} \right] \frac{\mathbf{v}}{v}, \quad (9)$$

where  $M$  is the mass of a satellite moving with velocity  $\mathbf{v}$  in the density field  $\rho$  of some host,  $X = v/(\sqrt{2}\sigma)$  where  $\sigma$  is the local 1D velocity dispersion of the host, and  $\ln \Lambda$  is the Coulomb logarithm. This quantity is taken as

$$\ln \Lambda = \ln \left( \frac{r}{\epsilon} \right), \quad (10)$$

where we have followed Hashimoto et al. (2003) and used the instantaneous separation  $r$  in place of the maximum impact parameter originally advocated by Chandrasekhar. Hashimoto et al. (2003) showed that this choice gave a better reproduction of the orbital decay time-scale.

From this set of initial conditions, we run a live disruption forward – which of course self-consistently allows for the effects of dynamical friction – and see if it approaches the target coordinates at the Crossover Point closely enough. If not, we update  $\epsilon$  and re-run. Typically, 2 such iterations are needed. The tolerance with which the phase space coordinates are matched at the Crossover Point is  $1 \text{ kpc}$  and  $5 \text{ km s}^{-1}$ . We explore a grid of Sgr masses in the range  $10^{10}$  to  $10^{11}$  and choose  $r_s$  from the mass-concentration relation, whilst the length  $\epsilon$  is in the range 6 to 12.

Finally, we need to extract the velocity dispersion profiles from the simulations. We transform the Galactocentric coordinates of the particles into heliocentric ones, and thence obtain  $(\tilde{A}_\odot, \tilde{B}_\odot)$  for particles. In each of the bins in  $\tilde{A}_\odot$ , we fit a Gaussian to extract the velocity dispersion. This works well for the trailing arm, but the leading arm is messy. The leading debris shows several distinct particle groups in the space of  $(v_{\text{GSR}}, \tilde{A}_\odot)$  belonging to individual stripping epochs. To account for that, for the leading debris analysis, we fit 2 Gaussians, at each  $\tilde{A}_\odot$ .

### 3.4 Results of the N-body experiments

Fig. 11 displays the evolution of the Sgr orbit and the mass in its dark matter halo contained within the tidal radius. This shows the gamut of choices first articulated by Jiang & Binney (2000) and then amplified by Niederste-Ostholt et al. (2010). The Sgr could easily once have been as massive as  $10^{11} M_\odot$ , in which case it would have had an apocentric distance of  $\sim 110 \text{ kpc}$  as recently as 5 Gyr ago. However, if its initial dark matter mass is reduced to  $10^{10} M_\odot$ , then it must have been correspondingly closer at  $\sim 70 \text{ kpc}$ . Note that the Crossover Point – in essence, the first apocentre in the Law & Majewski (2010b) potential – is reached at slightly

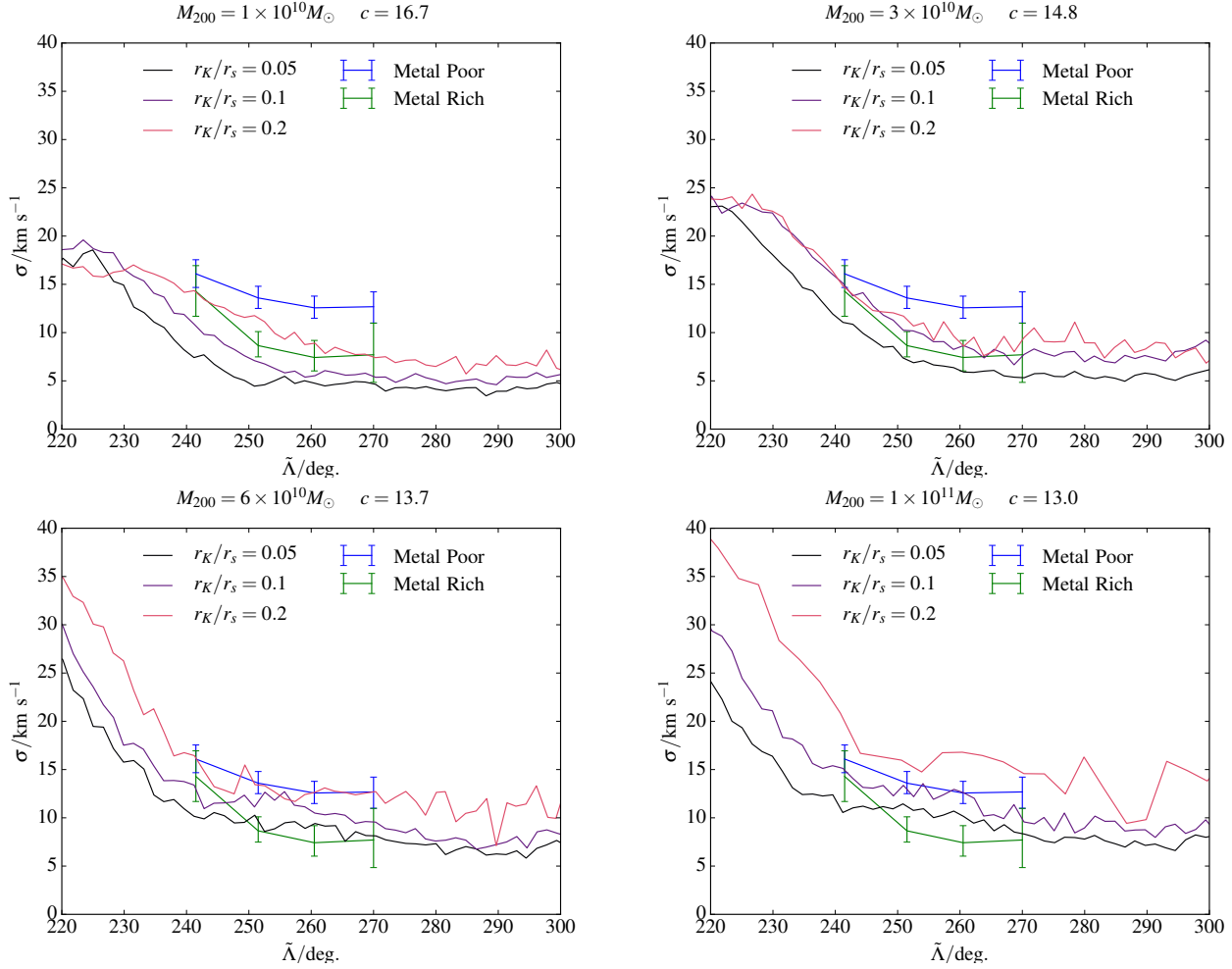


**Figure 13.** Velocity dispersion as a function of longitude in the trailing arm. Above each panel is marked the dark halo mass and concentration of the Sgr progenitor. The coloured lines show different ratios of King radius  $r_K$  to dark halo scalelength  $r_s$ , whilst the velocity dispersion data for the metal-poor and metal rich stars (measured in this work) are shown in blue and green respectively.

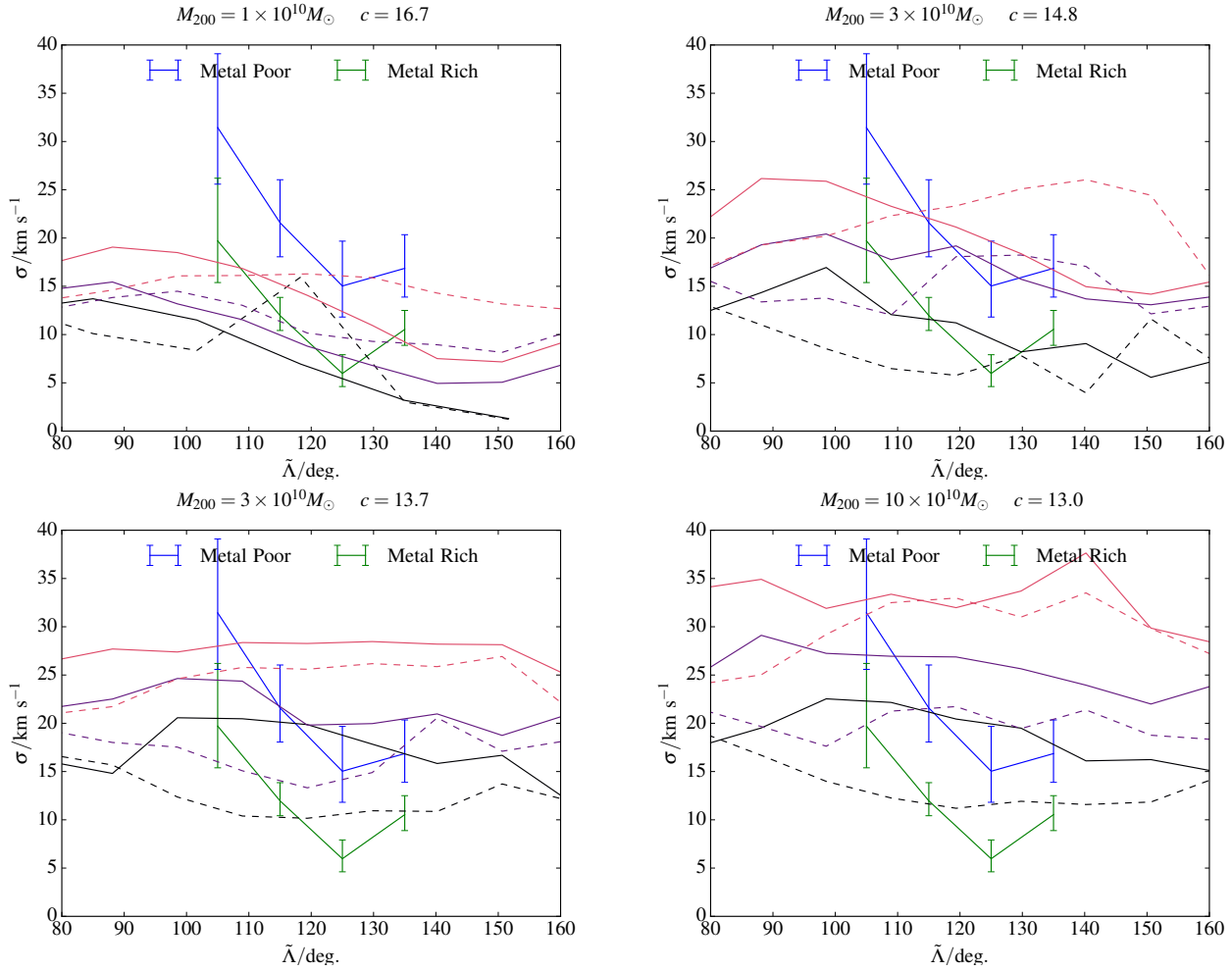
different epochs by progenitors with different masses. This is unsurprising, given different amount of dynamical friction, and hence, orbital evolution. The right panel illustrates the ruthlessness of the stripping process. The more massive the halo, the greater the efficacy of the stripping so that all the models end up with modern day remnants with dark matter mass  $\lesssim 10^9 M_\odot$ . There is a very small discontinuity in the run of the progenitor’s bound mass at the Crossover Point. This is due to the fact the Law & Majewski (2010b) MW is slightly denser, thus giving a smaller tidal radius for the Sgr dwarf at the same Galact-centric distance compared to the TF model.

Fig. 12 shows the behaviour of the luminous mass and velocity dispersion. Now, we have the freedom to vary not just the mass of the progenitor but also the embeddedness of the stellar light. Interestingly, the present day velocity dispersion is largely independent of the embeddedness as the curves in the upper panel converge at late times ( $\sim 5$  Gyr). If the progenitor mass is  $10^{10} M_\odot$ , then the velocity dispersion of the stars in the remnant is under  $10 \text{ km s}^{-1}$ . This rises to  $\sim 15 \text{ km s}^{-1}$  if the progenitor mass is  $6 \times 10^{10} M_\odot$ . In comparison, the first measurement of the velocity dispersion of giant stars in the Sgr remnant was by Ibata et al. (1997), who found  $11.4 \pm 0.7 \text{ km s}^{-1}$ . Later investigations confirmed that the Sgr remnant has a flat velocity dispersion profile with an amplitude of  $\sim 14$

$\text{km s}^{-1}$  out to  $10^\circ$  (see Fig. 11 of Frinchaboy et al. (2012)). However, caution is needed in comparing the velocity dispersion of the remnant in the simulations with the observations. In the initial set-up, the King profile was taken as a tracer density in eq. (4) and this may not be justifiable in the centre. Our approach is fine for the outer regions which form the tails, and so we now turn to these.

Please note that caution is required when comparing the results of our simulations directly to the data in hand. For example, it appears that both in terms of the DM mass shown in Fig. 11 and the stellar mass displayed in the bottom row of Fig. 12, the final state of the remnant is more depleted than it is implied by observations. More precisely, in the simulations, the final mass is lower than  $10^8 M_\odot$  and the remnant’s luminosity today is less than the half of the original stellar mass, while according to Majewski et al. (2013) the remnant’s mass should exceed  $10^8 M_\odot$ , and the Sgr has probably only lost 50% of its stars (see e.g. Niederste-Ostholt et al. 2010). However, while our choice of most of the model parameters is well motivated, plenty of freedom is still allowed. For example, the disruption time is probably uncertain at the level of 1 to 2 Gyrs. As such, the state of the progenitor 1 Gyr before the end of the simulation (as permitted by the current level of uncertainty) would match the observational constraints better.

Fig. 13 shows the run of velocity dispersions in the trailing



**Figure 14.** As Fig. 13, but for the leading stream. In the simulation, material stripped at different pericentric passages is distinguished by different line type. While the phase-space behaviour of the leading debris is markedly more complex as compared to the trailing one, it is re-assuring to see that our models reproduce the elevated velocity dispersions observed in the leading tail.

tail, compared to the data extracted in Section 2. In the surviving dSphs, such as Sculptor or Fornax, the half-light radius of the metal-rich population is a factor of  $\sim 2$  smaller than the metal-poor (see e.g., Amorisco & Evans 2012; Agnello & Evans 2012). The coloured lines refer to stellar populations in which the ratio  $r_K/r_s$  differs by successive factors of 2. So, it is reasonable to expect a good match between any successive pair and the data. Such is the case for the heavier mass progenitors with total dark halo mass  $\gtrsim 6 \times 10^{10} M_\odot$ . In both of the lower panels of Fig. 13, the match is encouraging especially given the limited number of models available to span the large parameter space. Progenitor masses  $\lesssim 3 \times 10^{10} M_\odot$  are unable to provide the hot metal-poor population. The trailing tail provides a reasonably clean test, but the picture is slightly more muddled when we turn to the leading tail in Fig. 14. Here, the two massive progenitors with mass  $6 \times 10^{10} M_\odot$  and  $10 \times 10^{10} M_\odot$ , match the data in all  $\tilde{\Lambda}_\odot$  bins in agreement with the trailing tail results. Additionally, in some (but not all) locations along the leading tail, the progenitor with  $3 \times 10^{10} M_\odot$  provides a reasonable fit. Note, however, that the leading tail simulations are significantly more cumbersome to interpret, as the line-of-sight velocity distribution is clearly multi-modal. This is evidenced by different behaviour of the solid and dashed lines representing the run

of the velocity dispersion in each sub-component in the simulated trailing tail.

## 4 DISCUSSION AND CONCLUSIONS

Multiple populations in dwarf spheroidals are known to be common. Dwarf extended star formation histories naturally produce younger, colder, more metal-rich populations and older, hotter, more metal-poor populations. According to this picture, we might expect the stripping process to remove predominantly metal-poor stars at first, but with an increasing admixture of metal-rich population as time goes by. Just as the multiple populations in dwarf spheroidals provide powerful constraints on the potential, so the multiple populations in the Sgr stream may be used to measure the mass of the Sgr progenitor's halo.

This paper has identified multiple sub-populations in the Sagittarius (Sgr) stream using the SDSS/SEGUE spectroscopic dataset. The metallicity distribution functions (MDFs) of both the leading and trailing arms have been decomposed into Gaussians representing metal-rich and metal-poor populations respectively. In this procedure, contamination of the sample by Milky Way halo stars is accounted for by constructing a data-driven empirical MDF

of the halo. We find that the MDF of the Sgr trailing stream is well represented by two Gaussians with means and dispersions  $(\mu_{\text{ST1}}^{[\text{Fe}/\text{H}]}, \sigma_{\text{ST1}}^{[\text{Fe}/\text{H}]}) = (-1.33, 0.27)$  and  $(\mu_{\text{ST2}}^{[\text{Fe}/\text{H}]}, \sigma_{\text{ST2}}^{[\text{Fe}/\text{H}]}) = (-0.74, 0.18)$  dex. In agreement with earlier studies (Sbordone et al. 2007; Koposov et al. 2013; de Boer et al. 2014), the trailing stream has a substantial metal-rich population. The leading stream's MDF can also be decomposed into two Gaussians with means and dispersions  $(\mu_{\text{SL1}}^{[\text{Fe}/\text{H}]}, \sigma_{\text{SL1}}^{[\text{Fe}/\text{H}]}) = (-1.39, 0.22)$  and  $(\mu_{\text{SL2}}^{[\text{Fe}/\text{H}]}, \sigma_{\text{SL2}}^{[\text{Fe}/\text{H}]}) = (-1.00, 0.34)$ . We find that - as seen by the SDSS/SEGUE - the metal-rich population in the leading stream is less prominent.

We link the different metallicity components to their kinematics by determining the mean velocity and dispersion of the sub-populations as a function of longitude along the stream. In all the longitude bins and for both tails, the metal-poor population has a larger velocity dispersion than the metal-rich. For the trailing tail, the metal-rich sub-population has kinematics well approximated by a Gaussian with  $\sigma_{\text{ST2}}^v \sim 8 \text{ km s}^{-1}$ , in accord with the results of Monaco et al. (2007) using high resolution spectroscopy of M-giant stars. The metal-poor component is hotter with  $\sigma_{\text{ST1}}^v \sim 13 \text{ km s}^{-1}$ , similar to the value found by Koposov et al. (2013). These values show modest variation with longitude. However, the dispersion of the Sgr leading stream depends more strongly on longitude. We find  $15 \text{ km s}^{-1} < \sigma_{\text{SL1}}^v < 30 \text{ km s}^{-1}$  for the metal-poor sub-population, and  $6 \text{ km s}^{-1} < \sigma_{\text{SL2}}^v < 20 \text{ km s}^{-1}$  for the metal-rich. Some of the variation is produced by projection effects, though some is produced by feathering or streamlets and some by orbital evolution of the stream in the host potential.

As the velocity dispersions for both populations in both tails can be measured across a swathe of longitudes, this gives a powerful constraint on the mass of the progenitor. By carrying out simulations of the disruption of Sgr in the Milky Way, we find that the starting Sgr mass has to be  $\gtrsim 6 \times 10^{10} M_{\odot}$ . If the mass is less than this, then the velocity dispersion of the simulated metal-poor stream is too low, irrespective of the embeddedness of the population in the original progenitor.

Such a high mass for the Sgr is consistent with a number of other lines of evidence. For example, models of Garrison-Kimmel et al. (2016) would predict a mass consistent with  $10^{11}$  for Sgr when using the determination of the total progenitor luminosity of  $\sim 10^8 L_{\odot}$  from Niederste-Ostholt et al. (2010). Moreover, the metallicity of the “knee” in the distribution of the abundance of  $\alpha$  elements at given [Fe/H] most likely - albeit in an indirect way - correlates with the mass of the dwarf galaxy. As shown by de Boer et al. (2014), the  $\alpha$ -knee in the Sgr dSph is just under that of the LMC, thus confirming the Sgr's ranking as the next most massive dwarf after the Magellanic Clouds. Note that the LMC itself has been recently estimated to have at least  $10^{11} M_{\odot}$  in DM, or perhaps even more (see e.g. Peñarrubia et al. 2016; Jethwa et al. 2016). The number of globular clusters (or, more precisely, their total mass) the galaxy hosts is also known to scale with its DM mass (Hudson et al. 2014). There are probably at least 8 GCs associated with the Sgr dwarf according to Law & Majewski (2010a), i.e. the same number the SMC hosts and half of the known contingent of the LMC.

The gap between the values of the progenitor's mass suggested by our study and those assumed so far as part of the disruption modelling (see e.g. Law & Majewski 2010b; Gibbons et al. 2014) is at least two orders of magnitude. The difference might actually be a lot less frightening as the value relevant for the stream centroid analysis is that at the onset of the stripping of the stellar compo-

nent. As evidenced in Fig. 12, the disruption of the luminous portion of the dwarf starts in earnest at least  $\sim 1$  Gyr after passing the Crossover Point. By then, more than 90% of the DM mass is gone, thus bringing the total progenitor's mass much closer to  $10^9 M_{\odot}$ . Note that the DM the Sgr has shed might play an important role in the reconstruction of the MW gravitational potential: in the end, an amount of the DM dumped onto the Galaxy in the plane perpendicular to the Galactic disk is at least the mass of the disk itself! The Sgr DM debris could represent the most significant halo substructure in the Galaxy today, thus affecting the interpretation the DM direct searches (see e.g. Freese et al. 2013; O'Hare & Green 2014).

Our work also has implications for the Milky Way warp. The idea that the tidal interaction of large satellite galaxies may excite warps has been proposed before, often with the suggestion that the Magellanic Clouds may be the culprit (e.g., Hunter & Toomre 1969; Weinberg & Blitz 2006). This is unlikely if the Magellanic are on first infall, which is the most likely interpretation of the proper motion data (Besla et al. 2007; Kallivayalil et al. 2013). If so, then another thuggish intruder into the Milky Way halo needs to be sought. A corollary of making the Sgr much more massive is that the havoc it wrought in the Milky Way disk is much more extensive. So, the Sgr must surely be the major suspect into ongoing enquiries as to the cause of the warp.

## ACKNOWLEDGEMENTS

SG thanks the Science and Technology Facilities Council (STFC) for the award of a studentship. The research leading to these results has received funding from the European Research Council under the European Union's Seventh Framework Programme (FP/2007-2013) / ERC Grant Agreement no. 308024.

## REFERENCES

- Agnello A., Evans N. W., 2012, *ApJ*, 754, L39  
Ahn C. P., Alexandroff R., Allende Prieto C., Anderson S. F., Anderton T., Andrews B. H., Aubourg É., Bailey S., Balbinot E., Barnes R., et al. 2012, *ApJS*, 203, 21  
Allende Prieto C., Sivarani T., Beers T. C., Lee Y. S., Koesterke L., Shetrone M., Sneden C., Lambert D. L., Wilhelm R., Rockosi C. M., Lai D. K., Yanny B., Ivans I. I., Johnson J. A., Aoki W., Bailer-Jones C. A. L., Re Fiorentin P., 2008, *AJ*, 136, 2070  
Amorisco N. C., 2015, *MNRAS*, 450, 575  
Amorisco N. C., Evans N. W., 2011, *MNRAS*, 411, 2118  
Amorisco N. C., Evans N. W., 2012, *MNRAS*, 419, 184  
Beers T. C., Carollo D., Ivezić Ž., An D., Chiba M., Norris J. E., Freeman K. C., Lee Y. S., Munn J. A., Re Fiorentin P., Sivarani T., Wilhelm R., Yanny B., York D. G., 2012, *ApJ*, 746, 34  
Behroozi P. S., Conroy C., Wechsler R. H., 2010, *ApJ*, 717, 379  
Bellazzini M., Correnti M., Ferraro F. R., Monaco L., Montegriffo P., 2006, *A&A*, 446, L1  
Belokurov V., Koposov S. E., Evans N. W., Peñarrubia J., Irwin M. J., Smith M. C., Lewis G. F., Gieles M., Wilkinson M. I., Gilmore G., Olszewski E. W., Niederste-Ostholt M., 2014, *MNRAS*, 437, 116  
Besla G., Kallivayalil N., Hernquist L., Robertson B., Cox T. J., van der Marel R. P., Alcock C., 2007, *ApJ*, 668, 949  
Binney J., Tremaine S., 2008, *Galactic Dynamics: Second Edition*. Princeton University Press

- Bressan A., Marigo P., Girardi L., Salasnich B., Dal Cero C., Rubele S., Nanni A., 2012, *MNRAS*, 427, 127
- Burkert A., 2015, *ApJ*, 808, 158
- Chandrasekhar S., 1960, *Principles of stellar dynamics*
- Chou M.-Y., Cunha K., Majewski S. R., Smith V. V., Patterson R. J., Martínez-Delgado D., Geisler D., 2010, *ApJ*, 708, 1290
- Conroy C., Wechsler R. H., 2009, *ApJ*, 696, 620
- de Boer T. J. L., Belokurov V., Beers T. C., Lee Y. S., 2014, *MNRAS*, 443, 658
- de Boer T. J. L., Belokurov V., Koposov S., 2015, *MNRAS*, 451, 3489
- Deason A. J., Belokurov V., Evans N. W., 2011, *MNRAS*, 416, 2903
- Diemer B., More S., Kravtsov A. V., 2013, *ApJ*, 766, 25
- Duffau S., Zinn R., Vivas A. K., Carraro G., Méndez R. A., Winnick R., Gallart C., 2006, *ApJ*, 636, L97
- Erkal D., Sanders J. L., Belokurov V., 2016, *ArXiv e-prints*
- Fernández-Alvar E., Allende Prieto C., Schlesinger K. J., Beers T. C., Robin A. C., Schneider D. P., Lee Y. S., Bizyaev D., Ebelke G., Malanushenko E., Malanushenko V., Oravetz D., Pan K., Simmons A., 2015, *A&A*, 577, A81
- Freese K., Lisanti M., Savage C., 2013, *Reviews of Modern Physics*, 85, 1561
- Frinchaboy P. M., Majewski S. R., Muñoz R. R., Law D. R., Łokas E. L., Kunkel W. E., Patterson R. J., Johnston K. V., 2012, *ApJ*, 756, 74
- Garrison-Kimmel S., Bullock J. S., Boylan-Kolchin M., Bardwell E., 2016, *ArXiv e-prints*
- Gibbons S. L. J., Belokurov V., Evans N. W., 2014, *MNRAS*, 445, 3788
- Gómez F. A., White S. D. M., Marinacci F., Slater C. T., Grand R. J. J., Springel V., Pakmor R., 2016, *MNRAS*, 456, 2779
- Hashimoto Y., Funato Y., Makino J., 2003, *ApJ*, 582, 196
- Helmi A., 2008, *A&A Rev.*, 15, 145
- Hendel D., Johnston K. V., 2015, *MNRAS*, 454, 2472
- Hudson M. J., Harris G. L., Harris W. E., 2014, *ApJ*, 787, L5
- Hunter C., Toomre A., 1969, *ApJ*, 155, 747
- Ibata R. A., Wyse R. F. G., Gilmore G., Irwin M. J., Suntzeff N. B., 1997, *AJ*, 113, 634
- Janesh W., Morrison H. L., Ma Z., Rockosi C., Starkenburg E., Xue X. X., Rix H.-W., Harding P., Beers T. C., Johnson J., Lee Y. S., Schneider D. P., 2016, *ApJ*, 816, 80
- Jethwa P., Erkal D., Belokurov V., 2016, *MNRAS*
- Jiang I.-G., Binney J., 2000, *MNRAS*, 314, 468
- Johnston K. V., Sackett P. D., Bullock J. S., 2001, *ApJ*, 557, 137
- Jurić M., Ivezić Ž., Brooks A., Lupton R. H., Schlegel D., Finkbeiner D., Padmanabhan N., Bond N., Sesar B., Rockosi C. M., Knapp G. R., Gunn J. E., Sumi T., Schneider D. P., Barentine J. C., Brewington H. J., Brinkmann J., 2008, *ApJ*, 673, 864
- Kallivayalil N., van der Marel R. P., Besla G., Anderson J., Alcock C., 2013, *ApJ*, 764, 161
- Kazantzidis S., Magorrian J., Moore B., 2004, *ApJ*, 601, 37
- King I., 1962, *AJ*, 67, 471
- Kleyna J., Wilkinson M. I., Evans N. W., Gilmore G., Frayn C., 2002, *MNRAS*, 330, 792
- Koposov S. E., Belokurov V., Evans N. W., et. al. 2012, *ApJ*, 750, 80
- Koposov S. E., Belokurov V., Wyn Evans N., 2013, *ApJ*, 766, 79
- Law D. R., Majewski S. R., 2010a, *ApJ*, 718, 1128
- Law D. R., Majewski S. R., 2010b, *ApJ*, 714, 229
- Lee Y. S., Beers T. C., Allende Prieto C., Lai D. K., Rockosi C. M., Morrison H. L., Johnson J. A., An D., Sivarani T., Yanny B., 2011, *AJ*, 141, 90
- Lee Y. S., Beers T. C., Sivarani T., Allende Prieto C., Koesterke L., Wilhelm R., Re Fiorentin P., Bailer-Jones C. A. L., Norris J. E., Rockosi C. M., Yanny B., 2008, *AJ*, 136, 2022
- Macciò A. V., Dutton A. A., van den Bosch F. C., Moore B., Potter D., Stadel J., 2007, *MNRAS*, 378, 55
- Majewski S. R., Hasselquist S., Łokas E. L., Nidever D. L., Frinchaboy P. M., García Pérez A. E., Johnston K. V., Mészáros S., Shetrone M., 2013, *ApJ*, 777, L13
- Majewski S. R., Skrutskie M. F., Weinberg M. D., Ostheimer J. C., 2003, *ApJ*, 599, 1082
- Martínez-Delgado D., Peñarrubia J., Jurić M., Alfaro E. J., Ivezić Z., 2007, *ApJ*, 660, 1264
- Monaco L., Bellazzini M., Bonifacio P., Buzzoni A., Ferraro F. R., Marconi G., Sbordone L., Zaggia S., 2007, *A&A*, 464, 201
- Navarro J. F., Frenk C. S., White S. D. M., 1996, *ApJ*, 462, 563
- Newberg H. J., Yanny B., Cole N., Beers T. C., Re Fiorentin P., Schneider D. P., Wilhelm R., 2007, *ApJ*, 668, 221
- Newberg H. J., Yanny B., Willett B. A., 2009, *ApJ*, 700, L61
- Niederste-Ostholt M., Belokurov V., Evans N. W., 2012, *MNRAS*, 422, 207
- Niederste-Ostholt M., Belokurov V., Evans N. W., Peñarrubia J., 2010, *ApJ*, 712, 516
- O'Hare C. A. J., Green A. M., 2014, *Phys. Rev. D*, 90, 123511
- Peñarrubia J., Gómez F. A., Besla G., Erkal D., Ma Y.-Z., 2016, *MNRAS*, 456, L54
- Purcell C. W., Bullock J. S., Tollerud E. J., Rocha M., Chakrabarti S., 2011, *Nature*, 477, 301
- Sbordone L., Bonifacio P., Buonanno R., Marconi G., Monaco L., Zaggia S., 2007, *A&A*, 465, 815
- Schlaufman K. C., Rockosi C. M., Allende Prieto C., Beers T. C., Bizyaev D., Brewington H., Lee Y. S., Malanushenko V., Malanushenko E., Oravetz D., Pan K., Simmons A., Snedden S., Yanny B., 2009, *ApJ*, 703, 2177
- Smolinski J. P., Lee Y. S., Beers T. C., An D., Bickerton S. J., Johnson J. A., Loomis C. P., Rockosi C. M., Sivarani T., Yanny B., 2011, *AJ*, 141, 89
- Starkenburg E., Helmi A., Morrison H. L., Harding P., van Worden H., Mateo M., Olszewski E. W., Sivarani T., Norris J. E., Freeman K. C., Shtetman S. A., Dohm-Palmer R. C., Frey L., Oravetz D., 2009, *ApJ*, 698, 567
- Torrealba G., Catelan M., Drake A. J., Djorgovski S. G., McNaught R. H., Belokurov V., Koposov S., Graham M. J., Mahabal A., Larson S., Christensen E., 2015, *MNRAS*, 446, 2251
- Walker M. G., Mateo M., Olszewski E. W., Gnedin O. Y., Wang X., Sen B., Woodroffe M., 2007, *ApJ*, 667, L53
- Weinberg M. D., Blitz L., 2006, *ApJ*, 641, L33
- Wetzel A. R., Nagai D., 2015, *ApJ*, 808, 40
- Widrow L. M., Gardner S., Yanny B., Dodelson S., Chen H.-Y., 2012, *ApJ*, 750, L41
- Yanny B., Gardner S., 2013, *ApJ*, 777, 91
- Yanny B., Newberg H. J., Johnson J. A., Lee Y. S., Beers T. C., Bizyaev D., Brewington H., Fiorentin P. R., Harding P., Malanushenko E., Malanushenko V., Oravetz D., Pan K., Simmons A., Snedden S., 2009, *ApJ*, 700, 1282
- Yanny B., Rockosi C., Newberg H. J., Knapp G. R., Adelman-McCarthy J. K., Alcorn B., Allam S., Allende Prieto C., An D., Anderson K. S. J., Anderson S., Bailer-Jones C. A. L., Bastian S., 2009, *AJ*, 137, 4377